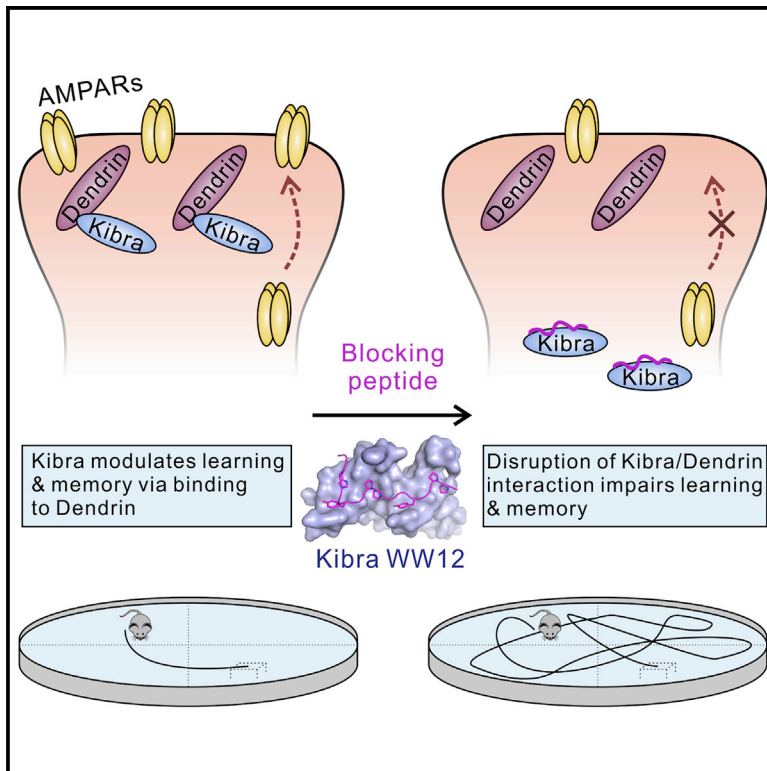**Article**

Kibra Modulates Learning and Memory via Binding to Dendrin

Graphical Abstract

Authors

Zeyang Ji, Hao Li, Zhou Yang, ...,
Zhijie Lin, Youming Lu, Mingjie Zhang

Correspondence

linzhijie@ust.hk (Z.L.),
lym@hust.edu.cn (Y.L.),
mzhang@ust.hk (M.Z.)

In Brief

Ji et al. report that the memory-related molecule Kibra, via its WW tandem domains, specifically binds to the synaptic protein Dendrin with a low-nanomolar dissociation constant to modulate spatial learning and memory.

Highlights

- Kibra WW tandem domains bind to Dendrin with low-nanomolar affinity

- Structure of Kibra WW domains bound to Dendrin PY motifs reveals the binding mechanism

- Disruption of the Kibra/Dendrin interaction impairs learning and memory in mice

- A Kibra mutation associated with Tourette syndrome causes defects in Dendrin binding

CellPress

Kibra Modulates Learning and Memory via Binding to Dendrin

Zeyang Ji,[1,5] Hao Li,[2,3,5] Zhou Yang,[1] Xian Huang,[2,3] Xiao Ke,[2,3] Sehui Ma,[2,3] Zhijie Lin,[1,*] Youming Lu,[2,3,*] and Mingjie Zhang[1,4,6,*]

[1]Division of Life Science, State Key Laboratory of Molecular Neuroscience, Hong Kong University of Science and Technology, Clear Water Bay, Kowloon, Hong Kong, China
[2]Department of Physiology, School of Basic Medicine and Tongji Medical College, Huazhong University of Science and Technology, Wuhan 4030030, China
[3]The Institute for Brain Research, Collaborative Innovation Center for Brain Science, Huazhong University of Science and Technology, Wuhan 430030, China
[4]Center of Systems Biology and Human Health, Hong Kong University of Science and Technology, Clear Water Bay, Kowloon, Hong Kong, China
[5]These authors contributed equally
[6]Lead Contact
*Correspondence: linzhijie@ust.hk (Z.L.), lym@hust.edu.cn (Y.L.), mzhang@ust.hk (M.Z.)
https://doi.org/10.1016/j.celrep.2019.01.097

SUMMARY

Kibra is a synaptic scaffold protein regulating learning and memory. Alterations of Kibra-encoding gene *WWC1* cause various neuronal disorders, including Alzheimer's disease and Tourette syndrome. However, the molecular mechanism underlying Kibra's function in neurons is poorly understood. Here we discover that Kibra, via its N-terminal WW12 tandem domains, binds to a postsynaptic density enriched protein, Dendrin, with a nanomolar dissociation constant. On the basis of the structure of Kibra WW12 in complex with Dendrin PY motifs, we developed a potent peptide inhibitor capable of specifically blocking the binding between Kibra and Dendrin in neurons. Systematic administration of the inhibitory peptide attenuated excitatory synaptic transmission, completely blocked long-term potentiation induction, and impaired spatial learning and memory. A Kibra mutation found in Tourette syndrome patients causes defects in binding to Dendrin. Thus, Kibra can modulate spatial learning and memory via binding to Dendrin.

INTRODUCTION

The memory-associated protein Kibra (kidney and brain expressed protein encoded by *WWC1*) was identified as a binding partner of the postsynaptic-enriched protein Dendrin in a yeast two-hybrid screening (Herb et al., 1997; Kremerskothen et al., 2003; Neuner-Jehle et al., 1996). Outside the nervous system, Kibra is involved in cell growth and organ size control, likely via the Hippo signaling pathway (Baumgartner et al., 2010; Duning et al., 2008; Genevet et al., 2010; Yoshihama et al., 2011; Yu et al., 2010). In the CNS, Kibra is highly expressed in brain regions that are associated with learning and memory (Papasso-

tiropoulos et al., 2006). Genetic variants of *WWC1* or Kibra protein level alterations were found in neurological disorders such as episodic memory impairments, cognitive function declines, depression, and Alzheimer's disease (Almeida et al., 2008; Galecki et al., 2010; Papassotiropoulos et al., 2006; Rodríguez-Rodríguez et al., 2009; Talarowska et al., 2016; Tracy et al., 2016; Zhang et al., 2009). Kibra deficiency in mice or rats reduces synaptic plasticity and impairs learning and memory (Heitz et al., 2016; Makuch et al., 2011; Vogt-Eisele et al., 2014). However, the cellular and molecular mechanisms underlying actions of Kibra in the brain are still unknown.

Kibra is a scaffold protein that contains an N-terminal WW domain tandem, a middle C2 domain, and a C-terminal PDZ binding motif (PBM) (Figure 1A). Kibra binds to PICK1 PDZ domain via its PDZ binding motif, thereby regulating synaptic trafficking of α-amino-3-hydroxy-5-methyl-4-isoxazolepropionic acid (AMPA) receptors (Makuch et al., 2011). A short motif preceding the PDZ binding motif of Kibra interacts with atypical protein kinases, including aPKCζ/ι/λ or PKMζ, which is a short and constitutively active isoform of aPKCζ (Vogt-Eisele et al., 2014; Yoshihama et al., 2011). Association of Kibra with PKMζ protects PKMζ from proteasome-mediated degradation and hence facilitates learning and memory (Vogt-Eisele et al., 2014). However, numerous proteins other than Kibra have been reported to bind to the PDZ domain of PICK1 (Xu and Xia, 2006–2007), and this raises the question of how Kibra specifically modulates memory performance via PICK1. Similarly, Kibra is expected to interact with all isoforms of aPKC instead of specifically with PKMζ in synapses. So why does Kibra specifically regulate only PKMζ but not the other aPKCs?

Dendrin is also enriched in postsynaptic densities in neurons (Elvira et al., 2006; Herb et al., 1997). Very little is known about Dendrin's function in neurons. In kidney, Dendrin is critical for the maintenance of the slit diaphragm, and re-localization of Dendrin from the slit diaphragm to the nucleus is known to promote podocyte apoptosis and kidney failure (Asanuma et al., 2007, 2011; Dunér et al., 2008; Patrakka et al., 2007; Weins
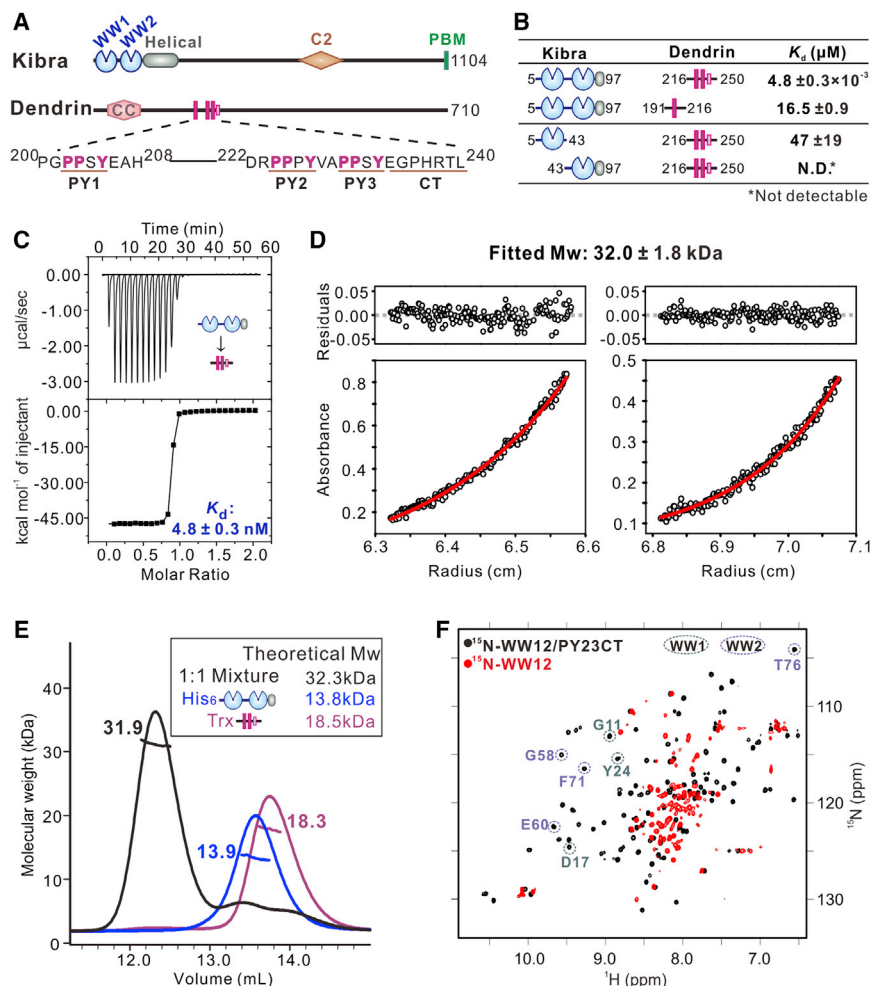
Figure 1. Kibra WW12 Binds to the PY Motifs of Dendrin with Super-Strong Affinity

(A) Schematic diagram showing the domain organizations of Kibra and Dendrin.

(B) ITC-based measurements of the binding affinities between Kibra WW domains and different PY motifs of Dendrin.

(C) An example ITC-based measurement of the binding between Kibra WW12 and Dendrin PY23CT showing super-strong binding with 1:1 stoichiometry.

(D) Analytical ultracentrifuge sedimentation equilibrium analysis of Kibra WW12/Dendrin PY23CT complex, showing that Kibra WW12 and Dendrin PY23CT form a stable 1:1 complex with a molecular mass of ~32 kDa in solution.

(E) Analytical gel filtration chromatography coupled with static light scattering analysis showing that Kibra WW12 and Dendrin PY23CT form a stable 1:1 complex in solution.

(F) Overlay of the ^{15}N-HSQC spectra of ^{15}N-labeled apo-Kibra WW12 (red) and in complex with unlabeled Dendrin PY23CT (black), showing binding-induced folding of Kibra WW12. Selective peaks from WW1 and WW2 are highlighted with dotted circles in teal and mauve, respectively. See also Figure S2.

Each K_d value is reported with a fitting error of the corresponding experimental binding curve. Also see Figure S1.

this inhibitory peptide reduces the synaptic expression of AMPA receptor channels, blocks the induction of long-term potentiation (LTP) of excitatory synaptic transmissions, and impairs learning and memory in mice. We also find that a Kibra W88C mutant occurring in Tourette syndrome patients destabilizes the Kibra WW tandem and weakens the Kibra-Dendrin complex formation *in vitro*.

RESULTS

Kibra WW Tandem Binds to Dendrin with a Low-Nanomolar Dissociation Constant

Kibra has two WW domains that are highly conserved during evolution (Figure S1A). An earlier work indicated that the WW domains of Kibra might bind to PY-motif peptides of Dendrin (Kremerskothen et al., 2003), but the detailed interaction between the two proteins was not characterized. Sequence analysis revealed that Dendrin contains three potential type I WW domain-binding PY motifs (PY1/2/3; Figure 1A), which are also conserved throughout evolution (Figure S1B). To determine a direct association between Kibra and Dendrin, we quantitatively analyzed binding affinities of the Kibra WW domains with various PY-motif combinations of Dendrin using purified proteins. Isothermal titration calorimetry (ITC)-based assay of the binding between the Kibra WW12 tandem (residues 5–97) and a Dendrin fragment containing all three PY motifs (PY123CT; residues 191–250, with "CT" denoting a seven-residue extension following PY3 that can enhance the

et al., 2015). But the functional implications of the interaction between Kibra and Dendrin in the brain are yet to be studied. Additionally, although WW domain-mediated protein-protein interactions are prevalent, such interactions are generally weak, with K_d values in the range of a few to a few dozen micromolar (Aragón et al., 2011; Chong et al., 2010; Kato et al., 2002, 2004). Each synapse contains many different WW domain proteins as well as numerous "PPXY" motif-containing proteins (the "PPXY" motif or PY motif is a well-known sequence to bind to WW domains; Kato et al., 2002; Schleinkofer et al., 2004). Thus, it is not clear whether the WW domain-mediated Kibra-Dendrin interaction would be specific enough to support their cellular functions.

Here, we discover that the WW tandem, but not each individual WW domain, of Kibra binds to a specific, two-PY-motif-containing sequence of Dendrin with an unprecedentedly high affinity ($K_d \sim 5$ nM) and specificity. Biochemical, nuclear magnetic resonance (NMR) spectroscopic, and X-ray crystallographic studies not only elucidated the mechanism governing the super-strong Kibra-Dendrin interaction but also allowed us to develop a short inhibitory peptide capable of effectively disrupting the Kibra-Dendrin interaction. We show that application of

binding affinity of Dendrin to Kibra, as discussed later) showed a two-phase binding process, which is obvious but difficult to derive accurate binding constants by curve fitting (Figure S1C). Given that PY2 and PY3 are adjacent to each other, we next separated the PY123CT into two fragments, PY1 and PY23CT, and measured their binding to Kibra WW12 using ITC. PY1 of Dendrin (residues 191–216) binds to Kibra WW12 with weak affinity typical of WW domains ($K_d \sim 17 \ \mu$M; Figure 1B), but PY23CT (residues 216–250) was found to bind to Kibra WW12 with an unexpectedly high affinity ($K_d \sim 5$ nM) and 1:1 stoichiometry by size-exclusion chromatography and analytical ultracentrifugation analyses (Figures 1C–1E). The ~3,000-fold binding affinity difference indicates that PY23CT instead of PY1 is responsible for the direct binding of Dendrin to Kibra WW12. Interestingly, Kibra WW12 binds to Dendrin PY23CT with affinity ~10,000-fold higher than does isolated WW1 ($K_d \sim 47 \ \mu$M; Figure 1B), whereas isolated WW2 has no detectable binding to PY23CT (Figure 1B). Strikingly, the Kibra WW12 and Dendrin PY23CT interaction discovered here is at least several hundred-fold stronger than known WW domain-mediated target bindings, suggesting that the interaction between Kibra and Dendrin may be mediated by a previously unknown mode. These biochemical data indicate that the two WW domains in the Kibra WW12 tandem function synergistically in binding to Dendrin PY23CT with super-high affinity, and the binding between Kibra and Dendrin is likely mediated by a previously unknown structural mode.

Dendrin PY23CT Binding-Induced Folding of Kibra WW12

We next characterized the binding between Kibra WW12 and Dendrin PY23CT using NMR spectroscopy. The ^{1}H-^{15}N heteronuclear single quantum coherence (HSQC) spectrum of Kibra WW12 was very inhomogeneous, suggesting a partially unfolded conformation of the tandem (Figures 1F and S2A). The ^{1}H-^{15}N HSQC spectrum of the isolated Kibra WW1 (residues 5–43) indicated that WW1 is well folded (Figure S2B). In contrast, the ^{1}H-^{15}N HSQC spectrum of Kibra WW2 (residues 43–97, purified as the Trx-fused protein because the isolated WW2 is very unstable) indicated that the WW2 domain is largely unfolded (Figure S2C). The broadening as well as small shifting of the backbone amide peaks in the Kibra WW12 ^{1}H-^{15}N HSQC spectrum with respected to those in the isolated WW1 and WW2 spectra suggested that the two WW domains in the tandem transiently interact with each other (Figure S2D). Upon binding to Dendrin PY23CT, the entire ^{1}H-^{15}N HSQC spectrum of Kibra WW12 underwent dramatic chemical-shift changes and became highly homogeneous and well dispersed (Figures 1F and S2E), indicating that Kibra WW12 becomes well folded upon binding to Dendrin PY23CT. We completed the backbone resonance assignment of Kibra WW12 in complex with PY23CT, and the results indicated that the complex was stable and homogeneous in conformation (Figure S2E). The chemical shift assignment also acted as the base for the structure and function analysis of Kibra WW12 tandem described below.

Structure of the WW12 Tandem in Complex with the PY23CT Motif

To understand the molecular basis governing super-strong Kibra-Dendrin binding, we solved the high-resolution structure of Kibra

WW12 in complex with Dendrin PY23CT using X-ray crystallography (Figures 2A and S3A; Table S1). In the crystal, WW12 adopts a domain-swapped dimer with the swapping site in residues 49–53 in the WW1 and WW2 linker (Figures S3A and S3B). An elongated helix (α2, residues 85–127) at the C-terminal end of WW12 forms a parallel coiled coil and appears to stabilize the domain-swapped dimer structure of Kibra WW12 (Figure S3A). Our analytical ultracentrifugation and gel filtration chromatography studies showed that Kibra WW12 in complex with Dendrin PY23CT adopts as a monomer (i.e., the complex is a 1:1 heterodimer; Figures 1D and 1E), suggesting that the dimer-of-dimer form of the complex seen in the crystal structure is likely resulted from the crystal packing. We further demonstrated using NMR spectroscopy that in solution, the α2 of WW12 in the complex is much shorter (i.e., stable up to residue E93 on the basis of the ^{1}H-^{15}N heteronuclear nuclear Overhauser effect [NOE] values, as shown in Figure 2B), indicating that the elongated coiled-coil dimer of α2 is a crystal-packing artifact. With the above analysis, we built a Kibra WW12/Dendrin PY23CT hetero-dimer structure by converting the swapped WW12 dimer into a monomer at the domain-swapping site (Figure S3C).

In the complex, the two WW domains interact with each other side by side in a back-to-front manner (i.e., the back side of WW1 interacts with the front of WW2) forming an integral supramodule (Figure 2A). With this interaction mode, the two canonical PY-motif binding grooves of the WW tandem are perfectly aligned to accommodate PY2 and PY3 of Dendrin, which are separated by only two residues (Figure 2A; see Figure 3 for more details). Interestingly, the direct interaction between the two canonical WW domains is minimal. Instead, the inter-domain linker (residues I35–L57) and the C-terminal α2 helix extension interact extensively with each other via numerous hydrophobic interactions (by I35, P44, L45, F47, A48, L55, P56, and L57 from the linker and W88 from α2), which are further complemented by several charge-charge and hydrogen bond interactions (e.g., the D53-R85-D83 network and the E82-R90 charge pair) (Figure 2A). Given that WW2 is largely unfolded in apo-WW12, it is envisioned that the binding of PY23CT induces the folding of WW2 and formation of the hydrophobic core "stitching" the two WW domains into an integral structural supramodule (Figure 2A). The ^{1}H-^{15}N heteronuclear NOE analysis showed that the residues from the inter-domain linker and residues from R85 to E93 at the C-terminal extension of WW2 are all well structured (Figure 2B). Consistent with this analysis, substitution of I35 in the inter-domain linker with Asp or deletion of the α2 helix from Kibra WW12 significantly decreased its binding to Dendrin PY23CT (Figure 2C). Substitution of the bulky W88 with a smaller aliphatic residue Ala also decreased WW12's binding to PY23CT (Figure 2C).

Dendrin PY23CT binds to Kibra WW12 in an antiparallel manner, with PY2 binding to WW2 and PY3CT to WW1. Both WW domains are typical type I domains, which can bind to the signature "PPXY"-motif sequence (Schleinkofer et al., 2004). Briefly, the two Pro residues in the "PPXY" motif of the ligand are sandwiched by two aromatic residues (e.g., Y23 from β2 and W34 immediately following β3 in WW1), and the Tyr in the PY motif is fixed by forming a strong hydrogen bond with a His in the β2/β3-loop of the WW domain (e.g., H27 in WW1). The
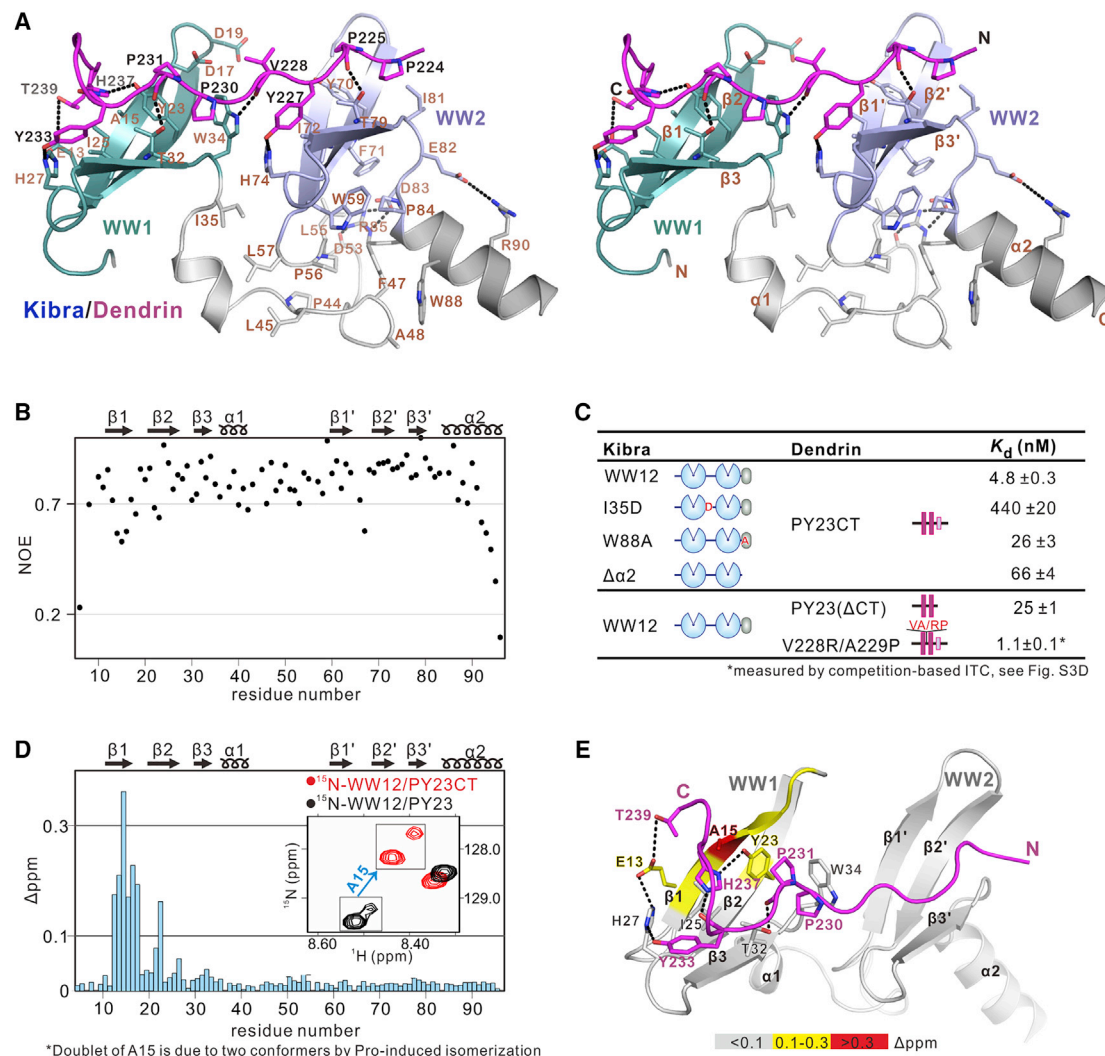
Figure 2. Structure of Kibra WW12 in Complex with Dendrin PY23CT

(A) Stereo view showing the detailed interaction of the Kibra WW12/Dendrin PY23CT complex. See also Figure S3 and Table S1.

(B) Plot of the ^1H-^{15}N heteronuclear NOE as the function of the residue number of ^{15}N-Kibra WW12 in complex with Dendrin PY23CT.

(C) ITC-based measurements comparing the binding affinities between Kibra WW12 (WT and various mutants) and different variants of Dendrin PY23CT.

(D) Plot of the backbone chemical shift differences as the function of the residue number of ^{15}N-Kibra WW12 in binding to Dendrin PY23CT and to Dendrin PY23 peptides. The chemical shift difference (Δppm) was calculated as Δppm $= \sqrt{(\Delta H)^2 + (0.17 \times \Delta N)^2}$. The inset is a portion of ^{15}N-HSQC spectra of the ^{15}N-Kibra WW12 showing that A15 in WW1 shows a large chemical shift difference upon binding to Dendrin PY23CT or to Dendrin PY23.

(E) Mapping the chemical shift differences in (D) onto the structure of Kibra WW12/Dendrin PY23CT complex.

Each K_d value is reported with a fitting error of the corresponding experimental binding curve. Also see Figures S2 and S3.

W34 equivalent in WW2 is I81 (Figure 2A). The Ile substitution for the defining Trp positioned at the C-terminal end of the type I WW domains presumably weakens the folding of WW2 and also likely explains why the isolated WW2 does not bind to PY23CT (Figure 1B). In addition to the two PY motifs, we observed that the seven-residue C-terminal extension following PY3 is also involved in binding to WW1 (see the specific interaction of H237 and T239 with a number of residues from WW1 shown in Figures 2D and 2E). NMR spectroscopic studies revealed that removal of the C-terminal extension from PY23CT induced obvious chemical-shift changes to a number of residues

in the WW1 that are in direct contact with CT of PY23CT seen in the crystal structure (Figures 2D and 2E), supporting that CT of PY23CT is directly involved in binding to WW12 in solution. Accordingly, removal of CT from PY23CT weakened its binding to WW12 by ~5-fold (Figure 2C).

During our structure analysis, we noticed that the side chains of D17 and D19 in the β1/β2 hairpin are facing the sidechain of V228 between PY2 and PY3 (Figure 2A). We replaced V228 of PY23CT with Arg, hoping to introduce charge-charge interaction(s) with D17 and/or D19 of WW12. We also replaced A229 with Pro to rigidify the backbone conformation of the linker.
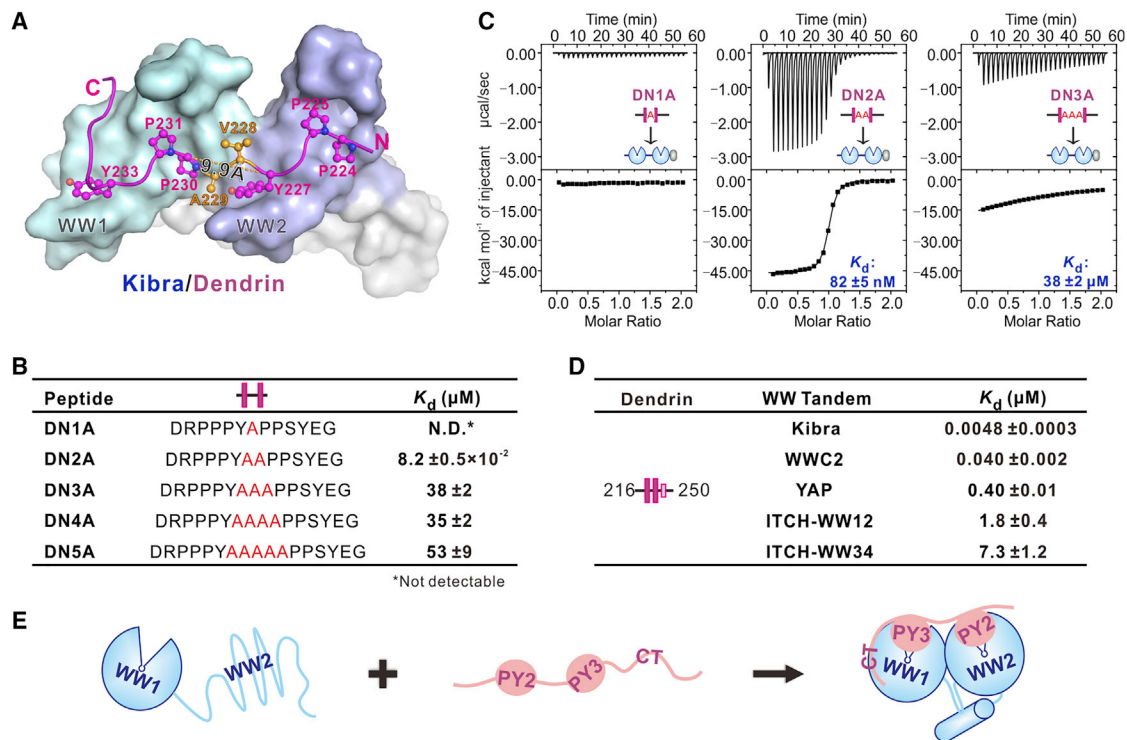
Figure 3. Structural Determinants of the Exquisite Binding between Kibra and Dendrin

(A) Formation of the WW12 supramodule in the Kibra WW12/Dendrin PY23CT complex defines the distance between the two PY motif binding sites of the WW tandem.

(B) ITC-based measurements comparing binding affinities between Kibra WW12 and Dendrin peptides with various insertion sequences between its two PY motifs.

(C) ITC-based measurements quantifying the binding of Kibra WW12 to DN1A, DN2A, and DN3A peptides, respectively.

(D) ITC-based measurements summarizing the binding between Dendrin PY23CT and various WW domain tandems from multiple WW domain-containing proteins, including WWC2, YAP, and ITCH.

(E) Schematic cartoon showing the Dendrin PY23CT peptide binding-induced folding of Kibra WW12 and subsequent stable complex formation.

Each K_d value is reported with a fitting error of the corresponding experimental binding curve. Also see Figure S4.

Satisfyingly, this "VA-to-RP" mutation further enhanced the mutant PY23CT peptide's binding to Kibra WW12 by ~5 fold ($K_d \sim 1$ nM; Figure 2C).

Determinants of Binding Specificity between Kibra and Dendrin

The super-strong interaction between Kibra WW12 and Dendrin PY23CT suggests that Kibra-Dendrin binding is very specific. An alternative possibility is that a pair of WW domains connected in tandem, which frequently occurs in WW domain-containing proteins, could bind to any two consecutive PY motifs with high affinity in general. We next determined which one of these scenarios might be true, as the answer has general implications in understanding target recognitions of many other multiple WW domain-containing proteins in addition to Kibra as well as for the functional studies of the Kibra-Dendrin interaction described later in this study.

The side-by-side and back-to-front alignment of WW1 and WW2 positions the two PY-motif binding sites of the tandem with a precise space (9.9 Å measured between Cα of Y227 in PY2 and Cα of Pro230 in PY3; Figure 3A), which matches nicely

to the length of two amino acid residues assuming an extended conformation. Thus, we predicted that the Kibra WW tandem is optimal in binding to two PY motifs separated by only two residues, such as Dendrin PY23CT. Shortening the linker of the two PY motifs should prevent the two PY motifs from simultaneously binding to the two WW domains. Lengthening the linker of the two PY motifs is also expected to weaken the binding because of the entropy costs from the linker. We decided to test this prediction using quantitative biophysical experiments. A series of Dendrin PY23-derived peptides with one to five Ala as the linker sequences (DN1A to DN5A; Figure 3B) were synthesized. We used ITC to measure the binding of these peptides to Kibra WW12 (Figures 3B and 3C). To save costs of the peptide synthesis, we removed the C-terminal extension from these peptides. Fitting our prediction, DN2A, which has two Ala between PY2 and PY3, binds to Kibra WW12 with the strongest binding affinity ($K_d \sim 82$ nM). When the linker length of PY23 increased to three or more residues, the binding of the peptides to WW12 decreased by >400-fold (Figures 3B and 3C). It is noticed that the binding affinities of the DN3A, DN4A, and DN5A peptides to Kibra WW12 are similar to that of the wild-type PY23CT peptide to WW1

(Figure 1B), suggesting that the peptides with longer linkers failed to induce WW12 supramodule formation and thus with much weaker WW12 binding affinities. Unexpectedly, the DN1A peptide showed almost no detectable binding to Kibra by ITC (Figure 3C; or extremely weak binding in NMR-based titration experiments shown in Figures S4A and S4C). We do not have an explanation for why the DN1A peptide has essentially no binding to Kibra WW12, as one would expect that the peptide should at least bind to WW1, as the other peptides do. The authenticity of DN1A peptide was validated using mass spectrometry (data not shown) and NMR spectroscopy (Figure S4B). We further showed that the DN1A peptide could bind to the isolated WW1 with affinity similar to the wild-type PY23CT does to WW1 ($K_d \sim 66$ μM; Figure S4C). Therefore, there is certain negative cooperation between the two PY motifs separated by only one residue, which prevents the DN1A peptide from binding to Kibra WW12. Taken together, the above biochemical and biophysical studies revealed that Kibra WW12 recognizes Dendrin PY23CT with extremely high specificity and requires the two PY motifs separated by two and only two amino acid residues.

A reverse scenario for the binding specificity between Kibra and Dendrin is whether the PY23CT might bind to the WW tandems from other WW tandem-containing proteins. To test this possibility, we measured the binding of Dendrin PY23CT to the WW12 tandem of WWC2, the isoform of Kibra. Given that WWC2 and Kibra share a very high sequence identity in their WW12 tandems ($\sim$90%; Figure S4D), Dendrin PY23CT also binds to WWC2 WW12 with very high affinity ($K_d \sim 40$ nM; Figure 3D). We tested two proteins, YAP as a representative of WW domain tandem proteins in the Hippo pathway and ITCH as a representative of the NEDD4 family WW tandem proteins, with their WW tandem sequences highly similar to that of Kibra WW12 (Figures S4E and S4F). ITC-based experiments showed that the YAP WW12 tandem binds to Dendrin PY23CT with a K_d of 400 nM, which is $\sim$80-fold weaker than Kibra WW12 does to PY23CT (Figure 3D). Both the WW12 and WW34 tandems of ITCH bind to Dendrin PY23CT with even weaker affinities (Figure 3D). With this analysis, we conclude that the unique Kibra WW12 tandem coupling renders extremely high binding affinity and specificity of Kibra WW12 toward Dendrin PY23CT.

In summary, the biochemical and structural studies reveal two key structural features responsible for the extremely high binding affinity and specificity between Kibra and Dendrin (Figure 3E). First, the binding of Dendrin PY23CT induces the folding of Kibra WW2 and subsequent formation of the WW12 supramodule, positioning the two PY motif binding sites at a precise distance and orientation. Second, the two PY motifs in Dendrin separated precisely by two residues are optimally suited for synergistically binding to the Kibra WW12 tandem. An extension sequence following the PY3 motif further enhances the binding of Dendrin to Kibra.

Inhibition of Kibra WW12 Tandem Defects Synaptic Transmission

Our discovery of PY23CT as a specific binding motif of Kibra WW12 indicates that a peptide fragment containing PY23CT sequence might be able to functionally disrupt the direct binding of Kibra to Dendrin. To test this hypothesis, we synthesized the PY23CT peptide and referred to it as the P_B peptide, for blocking

peptide. This peptide was used because it has unique advantages for studying functional interaction between Kibra and Dendrin over commonly used knockdown or knockout approaches. First, the P_B peptide does not interfere with any of the cellular functions of Kibra mediated by the rest of sequences outside the WW12 tandem (i.e., $\sim$90% of the protein; Figure 1A). Second, the P_B peptide inhibits the cellular function of Dendrin, mediated by a very short Kibra binding segment ($\sim$20 residues out of a total of 710 residues of the protein; Figure 1A) while preserving the functions of Dendrin mediated by the remaining sequence. We showed that the P_B and P_C peptides indeed neither interfered with the binding between Kibra and PATJ nor had any impact on the interaction between Dendrin and CIN85 (Figure S5C) (Duning et al., 2008; Li et al., 2018). To ensure the specific inhibition of the interaction between Kibra and Dendrin, we synthesized a mutant PY23CT peptide with only 2-residue changes (the Tyr in each PY motif, specifically Y227 and Y233, were replaced with Ala), referred to as the P_C peptide. The Y227/233A substitutions completely eliminated the binding between Kibra and the PY23CT peptide, and hence the P_C peptide was used as a control for the P_B peptide (Figure S3E).

Subsequently, we validated the specific targeting of the PY23CT peptide to Kibra in HeLa cells. mCherry-tagged full-length Kibra (mCherry-Kibra) was cytoplasmic and formed obvious condensed liquid droplets (Figures 4A and S5A). GFP-tagged PY23CT peptide (GFP-P_B) or the control peptide (GFP-P_C) was diffusely distributed with slight nuclear enrichment (Figure S5B). Upon co-expression, GFP-P_B, but not GFP-P_C, was recruited to the Kibra puncta in cytoplasm (Figures 4A and 4B). We also showed that GFP-DN1A peptide could hardly be recruited to the Kibra puncta when it was co-expressed with Kibra in HeLa cells (Figures 4A, 4B, and S5B), consistent with our biochemical data showing that there is minimal interaction between Kibra WW12 and the DN1A peptide (Figure 3B).

We next assessed the functional implications of the Kibra-Dendrin association in synaptic transmission. Neuronal cultures (day in vitro [DIV] 16) from the hippocampus of mice were treated with 5 μM of cell membrane-permeable TAT-conjugated P_B or P_C peptide (Figure 4C) or without any peptide as another control (Ct; Figure 4C). To minimize the TAT-peptide concentration for the inhibition of the Kibra-Dendrin interaction, we used the affinity-enhanced version of the P_B peptide, in which the two-residue linker ("VA") between the two PY motifs was replaced with "RP" (Figures 2C and 4C; the peptides are denoted as P_B' and P_C' peptides in Figures 4C–4E to reflect the subtle differences). Staining with antibodies against Kibra and MAP2 revealed that P_B' peptide treatment significantly reduced Kibra expression in dendritic shafts and spines, whereas neither P_C' peptide nor Ct treatment altered Kibra protein level (Figure 4C). Western blot analysis showed that Kibra protein in the fraction of plasma membrane, but not in the total cell lysates, was significantly reduced in the P_B' peptide treatment, compared with the controls (Figure 4D). Significantly, the reduced expression of Kibra in the plasma membrane was closely associated with a decrease in the expression of synaptic GluR1 and the number of synaptic spines (Figures 4E and S5D).

We next expressed the P_B or P_C peptide in CA1 pyramidal neurons of adult mice using the recombinant adeno-associated virus
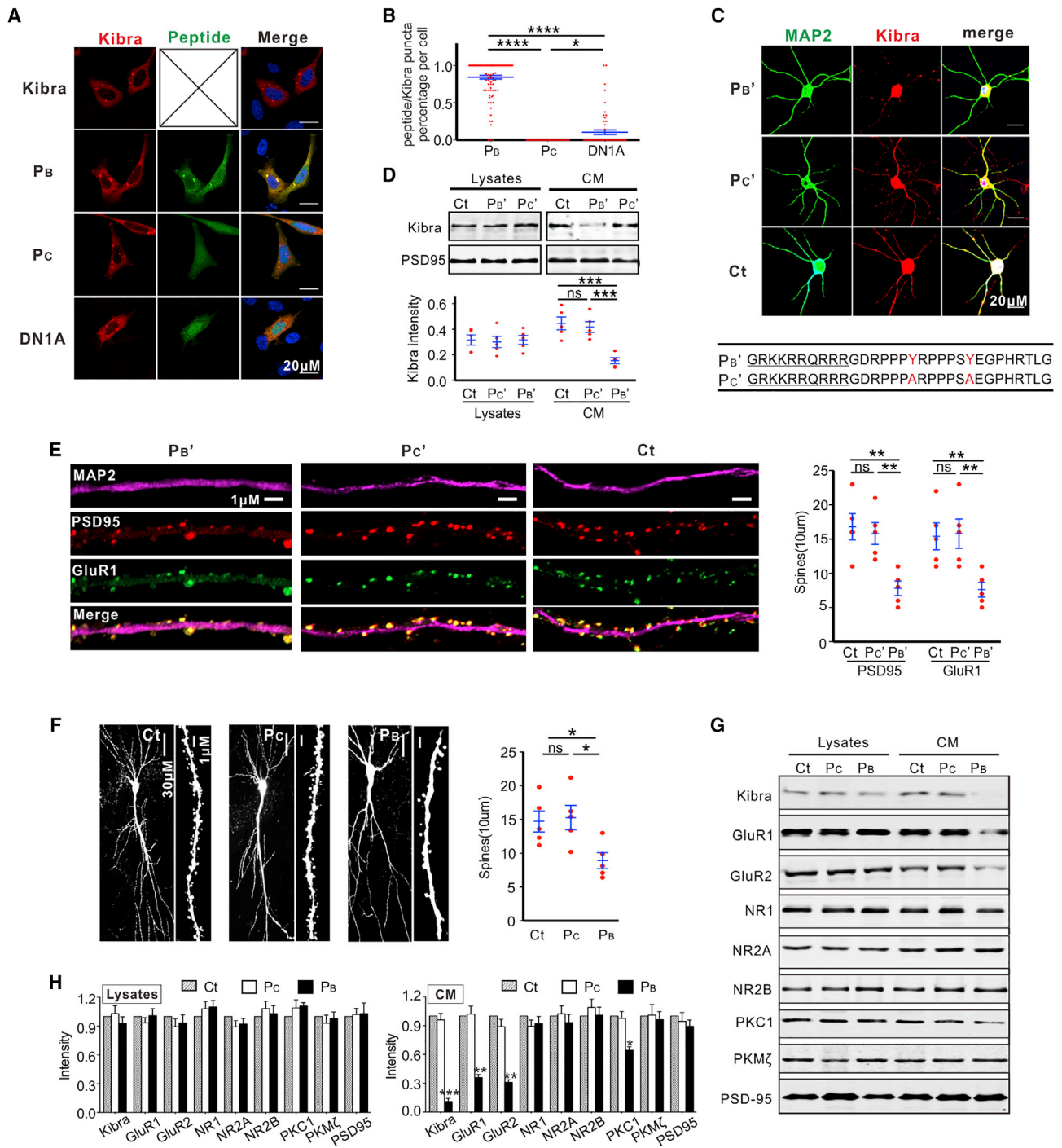
Figure 4. Inhibition of the WW12 Tandem Impairs Kibra Synaptic Targeting

(A) Representative fluorescent images of HeLa cells transiently co-expressing mCherry-tagged full-length Kibra and GFP-tagged peptides P_B, P_C, or DN1A, with cell nuclei stained with DAPI.

(B) Quantification of the percentage of GFP peptide-positive puncta co-localized with mCherry-Kibra puncta in HeLa cells co-expressing different GFP peptides with mCherry-Kibra. Data are expressed as mean ± SEM and were analyzed using GraphPad Prism 7 using one-way ANOVA followed by Tukey's multiple-comparisons test (*$p < 0.05$ and ****$p < 0.0001$). n(P_B) = 98, n(P_C) = 50, n(DN1A) = 59; n = numbers of HeLa cells obtained from three or more batches of experiments.

(C) Representative images of cultured neurons (16 DIV) from hippocampus of mice without (Ct) or with treatment of membrane-permeable P_B' or P_C' peptide at a concentration of 5 μM and stained with antibodies against MAP2 and Kibra, as indicated. Sequences of P_B' and P_C' peptide are shown below the images with the TAT sequence underlined.

(legend continued on next page)

(AAV) vector expressing the P_B peptide (AAV-CAG-P_B-GFP). In this study, expression of the P_C peptide (AAV-CAG-P_C-GFP) or GFP (AAV-CAG-GFP) was used as a control (Figure S5E). Consistent with the data from the cultured neurons, pyramidal neurons expressing P_B-GFP showed a significant reduction of spine numbers (Figure 4F). Expression of the P_B or P_C peptide did not alter the cell size of infected CA1 pyramidal neurons (Figure S5F). Additionally, expression of the P_B or P_C peptide neither changed the resting membrane potentials (RMPs) nor the input resistance (IR) of neurons (data not shown), indicating that neurons expressing either one of the peptides were healthy. Next, we prepared the membrane-associated fraction and the total cell lysates from the CA1 neurons expressing P_B-GFP, P_C-GFP, or GFP and probed with antibodies against Kibra and the major postsynaptic proteins including PSD-95 and AMPA receptor subunits. We found that the expression of P_B-GFP selectively attenuated the protein levels of Kibra, GluR1, GluR2, and PKC1 in the CM fraction but not in the total cell lysates (Figures 4G and 4H). Thus, inhibition of Kibra-Dendrin complex formation reduces synaptic targeting of Kibra and AMPA receptors and decreases the number of excitatory synapse in the brain of adult mice *in vivo*.

We next determined the impacts of the Kibra-Dendrin association in synaptic functions by analyzing the miniature excitatory postsynaptic currents (mEPSCs) and miniature inhibitory postsynaptic currents (mIPSCs) as well as the evoked EPSCs in CA1 pyramidal neurons of adult mice with the expression of P_B-GFP, P_C-GFP or GFP (Figures 5A and 5B). The mean amplitudes of the mEPSCs and the evoked EPSCs, but not the mIPSCs, in CA1 pyramidal neurons expressing P_B-GFP were significantly reduced compared with those expressing P_C-GFP or GFP. The frequencies of the mEPSCs did not change in all conditions (Figure 5A), showing an essential role of the Kibra-Dendrin association in excitatory synaptic transmission. It should be noted that the P_B peptide would also block additional Kibra WW tandem binding targets other than Dendrin if such target proteins indeed exist in neurons.

Blocking the Kibra/Dendrin Complex Formation Impairs Learning and Memory

The mutant mice lacking the *WWC1* gene that encodes Kibra protein displayed the partial deficits in LTP of excitatory synaptic transmissions (Heitz et al., 2016; Makuch et al., 2011), a main form of synaptic plasticity that is widely considered a cellular substrate of learning and memory (Bliss and Collingridge, 1993). Thus, we hypothesized that a role of Kibra in learning and memory is possibly mediated via its interaction with Dendrin. To test this hypothesis, the field excitatory synaptic potentials (fEPSPs) were recorded at the CA1 hippocampus from adult mice with the expression of P_B-GFP, P_C-GFP, or GFP, and LTP of fEPSPs was induced by a brief high-frequency stimulation (tetanus) of the afferent fibers (Figure 5C). Our data revealed that application of tetanus increased the mean amplitude of fEPSPs at CA1 neurons expressing either P_C-GFP or GFP, and this increase was sustained for more than 60 min. However, the same stimulation caused only a shorter time enhancement of the fEPSPs in neurons expressing P_B-GFP. This enhancement was decayed to the basal level within 15 min, showing that inhibition of the Kibra WW12 tandem by P_B-GFP completely blocks the induction of LTP at CA1 synapses.

Having determined the inhibitory effects of P_B-GFP in the LTP induction, we next trained adult mice with the expression of P_B-GFP, P_C-GFP, or GFP in the hidden platform version of the Morris water maze tests. We found that mice with the expression of P_B-GFP had a significant longer latency and swim-path length to reach the platform compared with those expressing P_C-GFP or GFP (Figure 5D). On probe trials, we then removed the hidden platform that was associated with the training session and allowed mice to search the pool for 90 s. Our data showed that mice expressing P_B-GFP lost their preference in searching for the target quadrant (Figure 5E). Together, these data reveal that the Kibra WW tandem via specifically binding to the Dendrin PY motifs plays an essential role in spatial information acquisition.

Silencing Dendrin Impairs Synaptic Transmission, Learning, and Memory

Our data described above suggest that Dendrin possibly acts as a binding substrate of Kibra for learning and memory (Figures 1 and 2). To test this possibility, we engineered the CA1 neurons of adult mice with the expression of a small interference RNA (siRNA) that specifically inhibits the Dendrin gene (siDDN; Figure S6A). A scrambled siDDN (ssiDDN) that did not affect the Dendrin expression was used as a control (Figure S6C). Silencing Dendrin in CA1 neurons of adult mice produced essentially the same effects as those caused by the inhibition of Kibra

---

(D) Immunoblotting images (top) of the cellular lysates and membrane fractions (CM) of cultured neurons (18 DIV) from the hippocampus of mice without (Ct) or with treatment of a membrane-permeable P_B' or P_C' peptide at a concentration of 5 μM. The cell lysates and CM fraction were isolated and blotted with antibodies against PSD95 and Kibra, as indicated. The intensity of individual Kibra blots was normalized to the respective PSD95 at Ct (defined as 1.0). Data are mean ± SEM (n = 5; ns, not significant; ***p < 0.001, t test).

(E) Representative images (left) showing dendritic branches from the cultured neurons without (Ct) or with treatment of a membrane-permeable P_B' or P_C' peptide at a concentration of 5 μM and stained with antibodies against GluR1, PSD95, and MAP2. The numbers of PSD95- and GluR1-labeled spines per 10 μm dendritic branches from the individual cultured neurons and their averages per group are plotted (right). Data are mean ± SEM (n = 5; ns, not significant; **p < 0.01, t test).

(F) Representative images (left) showing the individual CA1 pyramidal cells from mice brain and selected dendrites expressing eGFP (Ct), P_B, or P_C peptide using the AAV-CAG-eGFP, AAV-CAG-P_C-eGFP, or AAV-CAG-P_B-eGFP virus vectors. The numbers of spines in the dendritic branches of CA1 pyramidal neurons of the individual and their averages per group of mice are plotted (right). Data are mean ± SEM (n = 5; ns, not significant; *p < 0.05, t test).

(G) Representative images showing the blots of the cell lysates and membrane fraction (CM) prepared from the hippocampus of mice expressing P_C-GFP or P_B-GFP or eGFP (Ct) alone.

(H) The band intensities of the blots normalized to the respective control (Ct, defined as 1.0) are plotted. Data are mean ± SEM (n = 4 assays; *p < 0.05, **p < 0.01, and ***p < 0.001 compared with the respective controls, t test).
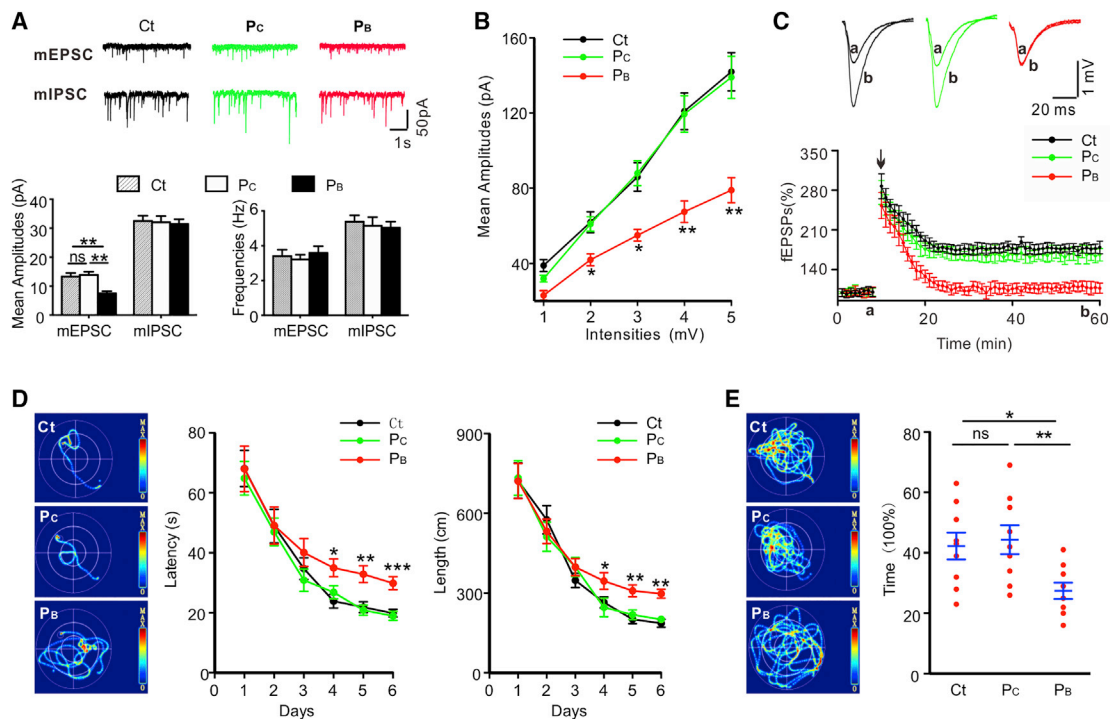
Also see Figure S5.

Figure 5. Inhibition of the Kibra WW Tandem Impairs LTP and Learning and Memory

(A) Representative recordings (top) show the mEPSCs and the mIPSCs in CA1 pyramidal neurons of the hippocampal slices from adult mice with the expression of P_C-GFP, P_B-GFP, or eGFP (Ct) alone. The mean amplitudes and frequencies of the mEPSCs versus the mIPSCs are plotted (bottom). Data are mean ± SEM (n = 12 recordings, six mice per group; ns, not significant; **p < 0.01, t test).

(B) The mean amplitudes of the evoked EPSCs are plotted against the stimulus intensities from 1 to 5 mV. The EPSCs are recorded at CA1 pyramidal neurons in the hippocampal slices from adult mice with the expression of P_C-GFP, P_B-GFP, or eGFP (Ct) alone. Data are mean ± SEM (n = 12 recordings, six mice per group; *p < 0.05 and **p < 0.01 compared with P_C-GFP, t test).

(C) Expression of P_B-eGFP blocks LTP induction. A plot shows the time course of the recordings of the fEPSP slope at CA1 synapses in the hippocampal slices from adult mice with the expression of P_C-GFP, P_B-GFP, or eGFP (Ct) alone. The slope (20%–80%) of the fEPSPs evoked by stimulation of the Schaffer-collateral fibers is normalized to the baseline (defined as 100%). The representative traces are the fEPSPs at basal line and 30 min after tetanus stimulation, as indicated with an arrow. Data are mean ± SEM (n = 12 recordings, six mice per group; ***p < 0.001 compared with control, t test).

(D) The average latency and swim length to reach a hidden platform are plotted against the blocks of trials (days) in Morris water maze tests. Data are mean ± SEM (n = 9 mice per group; *p < 0.05, **p < 0.01, and ***p < 0.001 compared with control, t test). Representative hotspots of path tracings are taken from training session at day 6.

(E) The percentage of time spent in a targeting quadrant during the probe trial from the individuals and their averages per group is plotted. Data are mean ± SEM (n = 9 mice per group; *p < 0.05 and **p < 0.01 compared with control, t test). Representative hotspots of path tracings are taken from the probe trial at day 8.

Also see Figure S5.

binding to Dendrin using the P_B peptide. Specifically, Dendrin gene silencing reduced synaptic AMPA receptor membrane targeting (Figures 6A and 6B), suppressed excitatory synapse transmission and LTP (Figures 6C and 6D), and defected spatial learning and memory (Figures 6E and 6F). Silencing Dendrin did not alter the resting membrane potentials and input resistance in the recording cells (Figure S6B), indicating that our RNAi-mediated manipulation of Dendrin did not affect the cell viability. Together, our data demonstrate that Kibra, via specific and super-tight binding to PSD-enriched Dendrin, plays essential roles in synaptic plasticity, learning, and memory.

A W88C Mutation of Kibra Impairs the Interaction of Kibra with Dendrin

A W88C mutation has been identified as a recurrent *de novo* variant of Kibra in Tourette syndrome with high confidence (Willsey et al., 2017). W88 is located at the start of α2 following WW2 and functions as a key residue for forming the hydrophobic interaction network stabilizing the Kibra WW12 supramodule (Figure 2A). The substitution of the bulky W88 with Cys is expected to weaken the coupling of α2 to the rest of the WW12 tandem (Figures 2A and 7A). Because the α2 helix is important for strong binding of Kibra WW12 to Dendrin, the W88C mutation of Kibra may weaken its binding to Dendrin. Additionally, structural analysis revealed that C50 in the inter-WW12 linker is in close vicinity with W88 (a distance of 8.4 Å between C50 Cβ and W88 Cβ; Figure 7A). Substitution of W88 with Cys may promote formation of an intra-molecular disulfide bond of the mutant Kibra, which could further perturb the inter-domain packing of the Kibra WW12 tandem and interfere its binding to Dendrin.

To test this probability, we characterized the structural perturbation of the Kibra WW12 tandem induced by the
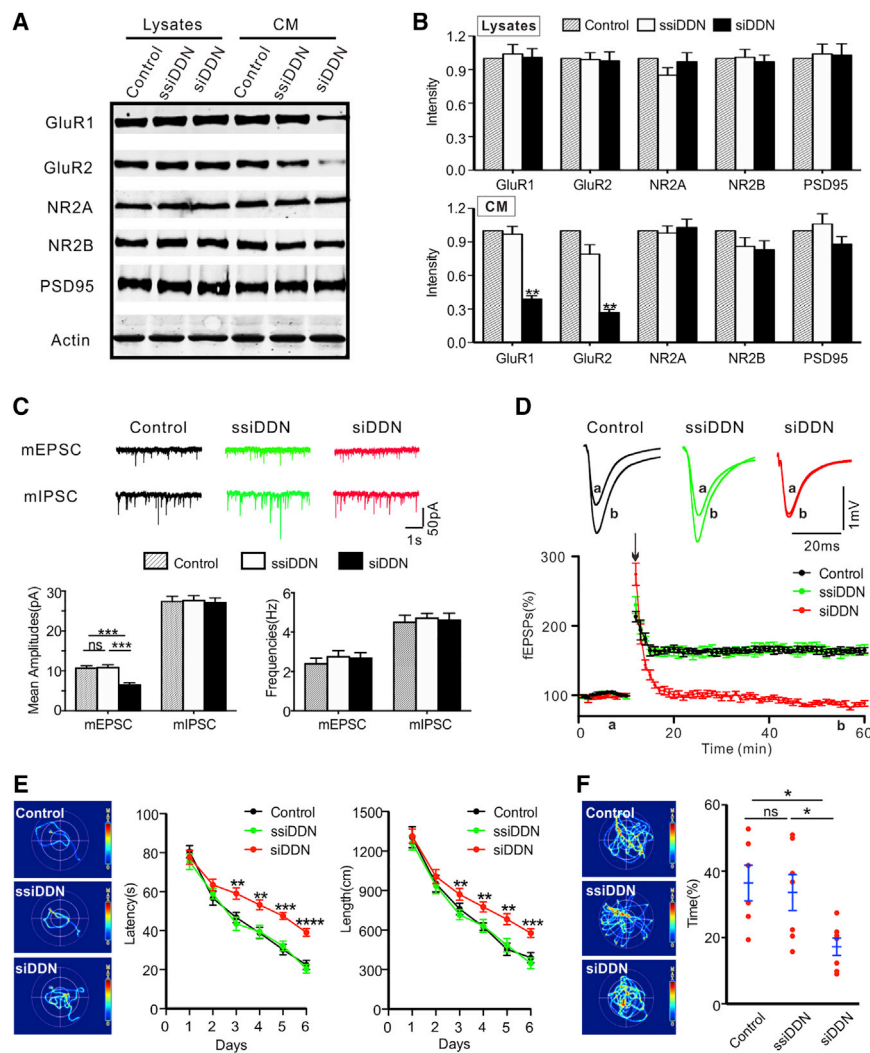
Figure 6. Silencing Dendrin Impairs LTP and Learning and Memory

(A) Cell lysates and CM fractions from the CA1 hippocampus of adult mice 4 weeks after the injection of saline (lane 1, control), Lenti-U6-ssiDDN-eGFP (lane 2, ssiDDN), or Lenti-U6-ssiDEN-eGFP (lane 3, siDDN) virus were isolated and blotted with antibodies, as indicated. The similar results were seen in each of the four experimental mice.

(B) The band intensities that were normalized to the respective control (defined as 1.0) from the lysates and CM fraction are plotted. Data are mean ± SEM (n = 4; **p < 0.01 compared to the respective controls, t test).

(C) Representative recordings (top) of the mEPSCs and the mIPSCs from CA1 pyramidal neurons in the hippocampal slices of adult mice without (control) or with the expression of either ssiDDN or siDDN. The mean amplitudes and frequencies of the mEPSCs and the mIPSCs are plotted (bottom). Data are mean ± SEM (n = 12 recordings, six mice per group; ns, not significant; ***p < 0.001, t test).

(D) Silencing Dendrin blocks the induction of LTP. The time course of the recordings of the fEPSP slope at CA1 synapses in the hippocampal slices from adult mice without (control) or with the expression of ssiDDN or siDDN is plotted. The slope of the fEPSPs evoked by stimulation of the Schaffer-collateral fibers is normalized to the baseline (defined as 100%). The representative traces are fEPSPs at basal line and 50 min after tetanus, as indicated with an arrow. Data are mean ± SEM (n = 12 recordings; six mice per group, t test).

(E) Silencing Dendrin impairs spatial learning and memory. The average latency and swim length to reach a hidden platform is plotted against the blocks of trials (days) in Morris water maze tests. Data are the mean ± SEM (n = 9 mice per group; **p < 0.01, ***p < 0.001, and ****p < 0.0001, t test). Representative hotspots of path tracings are taken from training session at day 6.

(F) The percentage of time spent in a targeting quadrant during the probe trial from the individuals and their averages per group is plotted. Data are mean ± SEM (n = 9 mice per group; *p < 0.05, t test). Representative hotspots of path tracings are taken from the probe trial at day 8.

Also see Figure S6.

W88C substitution. Comparison of the ^{1}H-^{15}N-HSQC spectra of PY23CT in complex with ^{15}N-labeled wild-type Kibra WW12 (WW12WT) or the mutant (WW12W88C) revealed that the mutant Kibra WW12 is still folded, and the two WW domains are largely intact (Figure 7B). However, careful analysis of the HSQC spectra revealed that compared with the wild-type protein, the W88C mutation led to disappearances of amide peaks corresponding to the residues from the α2 helix (Figure 7C, peaks with labeling in purple) and concomitant appearance of a set of new peaks characteristic of the random coil structure (Figure 7C, peaks highlighted with a purple dashed triangle). These newly appeared peaks in the HSQC spectrum of the mutant protein disappeared when the pH of the sample was raised to 8.0 (Figure 7C), indicating that these residues are indeed unstructured. This analysis indicated that the substitution of W88 with Cys led to unfolding of the α2 helix even when the mutant protein was in complex with Dendrin PY23CT. However, the

W88C mutation does not completely disrupt the folding and binding of Kibra WW12 to Dendrin.

Our subsequent ITC-based assay showed that the W88C mutation weakened Kibra's binding to Dendrin PY23CT by ∼6-fold (K_d from 4.8 to 30 nM; Figures 7D and S7B), a finding totally consistent with our structural analysis. We further demonstrated that the W88C mutant of Kibra WW12 can undergo spontaneous oxidation via formation of intra-molecular disulfide bond between C50 and C88, whereas the WT Kibra WW12 is much more resistant to Cys-mediated oxidation (Figures 7D and S7A). We further showed that the oxidized form of WW12W88C has an even lower affinity in binding to Dendrin PY23CT (K_d ∼ 154 nM; Figures 7D and S7B). Given that direct binding between Kibra and Dendrin is essential for learning and memory, the W88C mutation that causes Dendrin binding deficiency might contribute to the underlying mechanism of learning and memory deficits in patients with Tourette syndrome.
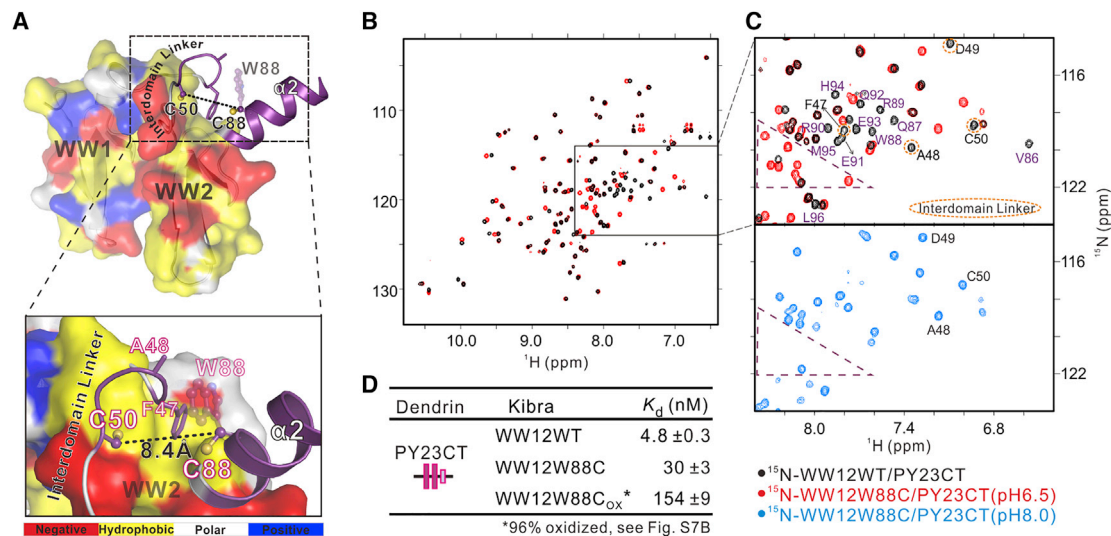
Figure 7. The W88C Mutation of Kibra Impairs Its Binding to Dendrin

(A) Surface combined with ribbon representation showing that W88 interacts with F47 and A48 from inter-domain linker thus stabilizing the Kibra WW12 supramodule. C50 from the WW12 inter-domain linker is near W88 (the Cβ of two residues are separated by 8.4 Å).

(B) Overlay of the ^{15}N-HSQC spectra of the ^{15}N-Kibra WW12WT (black) and ^{15}N- Kibra WW12W88C (red) in complex with unlabeled PY23CT.

(C) Top: a selected region of ^{15}N-HSQC spectra from (B), showing that residues from inter-domain linker (residues 47–50, dotted circles in orange) and α2 (residues 85–96, labeling in purple) undergo significant chemical-shift changes induce by the W88C substitution. A set of new peaks appeared (highlighted with a purple triangle) for the WW12W88C compared with the WT WW12. Bottom: the same region of the ^{15}N-HSQC spectrum of WW12W88C in complex with un-labeled Dendrin PY23CT as in (B), except that the pH of the sample was raised to 8.0. It is noted that the set of new peaks disappeared upon raising the pH of the complex sample.

(D) Summary of ITC-based measurement showing that the W88C mutation of the Kibra WW12 has a weaker binding to Dendrin. Oxidation of the WW12W88C further weakened its binding to Dendrin. Each K_d value is reported with a fitting error of the corresponding experimental binding curve.

Also see Figure S7.

Further experiments testing functional impacts of the W88C Kibra mutation in living neurons or mice will be required to substantiate the above biochemical findings.

DISCUSSION

In this study, we have revealed a previously unrecognized mode of tandem WW domain-mediated target recognition resulting in super-high binding affinity (low-nanomolar K_d) and specificity between Kibra and Dendrin. WW domain proteins and PY motif-containing proteins are prevalent in the proteomes of all metazoans. Bindings between an isolated WW domain and its PY motif-containing ligands are generally weak and promiscuous (Macias et al., 1996). Such low specific bindings apparently do not match with often very specific functions of WW domain-containing proteins or their binding targets. Earlier studies have shown that a pair of WW tandem can bind to multiple PY motifs with some synergism and raise the binding affinity (K_d) to as high as several hundred nanomolar (Aragón et al., 2011; Chong et al., 2010). Strikingly, direct binding between Kibra WW12 and Dendrin PY23CT is hundreds-fold stronger than the strongest WW tandem/target bindings reported and thousands-fold stronger than any individual WW/target binding known to date (Kato et al., 2002). We tested a number of tandem WW domains with high sequence similarities to Kibra WW12 and found that these WW tandems bind to Dendrin PY23CT with only moderate affinities. We further showed that removal or insertion of only one residue from or to the two PY motif linker abolished or dramatically weakened its binding to Kibra WW12, indicating that the specificity of the Kibra-Dendrin interaction is achieved by both the Kibra WW12 tandem and the specific PY motifs of Dendrin. The formation of the Kibra tandem supramodule is mediated by the sequences outside the two WW domains (Figure 2). Because the residues of Kibra WW12 inter-domain linker and the C-terminal α2 helix extension are unique to Kibra with respect to WW domains from other proteins, the Dendrin-induced formation of the Kibra WW12 tandem supramodule is likely to be specific, and thus the binding between Kibra and Dendrin is very specific.

Given that most of the WW domain-containing proteins contain multiple WW domains arranged in tandem, it is tempting to speculate that some of these WW tandems may also recognize their cognitive targets with very high affinity and specificity in order to match their physiological functions. Thus, we call for re-evaluation of WW tandem-mediated target interactions that were shown to have low or moderate affinities and specificities. This issue seems to be particularly relevant in the field of cell growth and polarity regulations, as many of the proteins involved in this filed contain multiple WW domains connected in tandem (Figure S4F). A large number of WW domain-mediated target bindings have been reported for these proteins, but it has been rare in the field in examining whether such interactions are truly specific.

In this study, we have generated a highly specific and super-strong Kibra-binding P_B peptide. This peptide has provided us with a unique tool to investigate the neuronal functions of Kibra and the interaction between Kibra and Dendrin in the brain *in vivo*. Kibra is a scaffold protein without recognizable enzymatic activities, and it is likely to function by assembling its different target proteins into large signaling complexes. In this regard, conventional approaches such as knockout or knockdown of Kibra may cause a concomitant loss of the associations of all Kibra-assembled target proteins and thus result in pleotropic outcomes with mechanisms that are difficult to discern. Additionally, genetic compensation between Kibra and WWC2 may cause another level of complication, and indeed, the mutant mice lacking the *WWC1* gene showed only a partial inhibition of LTP (Heitz et al., 2016; Makuch et al., 2011). Because of its specific binding to the Kibra WW12 tandem, the P_B peptide only blocks the interaction between Kibra and Dendrin, without interfering in other Kibra- and Dendrin-mediated protein-protein interactions. Using this peptide, we have demonstrated that a specific inhibition of the binding between Kibra and Dendrin attenuates AMPA receptor synapse targeting and synaptic transmission. Significantly, we have shown in adult mice that inhibition of the Kibra-Dendrin interaction completely blocks the induction of LTP and dramatically reduces the capacity of spatial information acquisition in Morris water maze tests. Consistent with the use of the inhibitory P_B peptide, we have also found that a mutation of Kibra that occurs in human patients with Tourette syndrome shows a significant deficiency in binding to Dendrin. Together, this study has demonstrated that Kibra physically and functionally interacts with Dendrin for the control of learning and memory and hence provided a molecular explanation for why Kibra mutations can cause the learning and memory deficits in human brain disorders such as Alzheimer's disease and Tourette syndrome.

Dendrin is a synaptic enriched protein, but its function remains unknown. In the present study we have shown that Dendrin contains a unique sequence of PY motifs that specifically binds to the WW12 tandem of Kibra. Disruption of this binding produces the inhibitory effects in synaptic functions and learning and memory. The same inhibition can be also achieved by silencing Dendrin gene using a siRNA. Thus, Dendrin acts as a binding substrate of Kibra for the control of spatial learning and memory. It should be pointed out that the Kibra WW12 tandem may bind to additional PY motif-containing target proteins other than -Dendrin in neurons. The P_B peptide used here would also block the interaction of Kibra with these target proteins.

STAR★METHODS

Detailed methods are provided in the online version of this paper and include the following:

- KEY RESOURCES TABLE
- CONTACT FOR REAGENT AND RESOURCE SHARING
- EXPERIMENTAL MODEL AND SUBJECT DETAILS
  - HeLa Cells and HEK293T Cells Culture
  - Primary Neuronal Culture
  - Animals

- METHOD DETAILS
  - Plasmid Construction, Protein Expression and Purification
  - Isothermal Titration Calorimetry Assay
  - Analytical Gel Filtration Chromatography Coupled with Static Light Scattering
  - Crystallography
  - NMR Experiments
  - Cell Cultures and Imaging
  - Stereotaxic Injection
  - Western Blots and Staining
  - Morris Water Maze Tests
  - Electrophysiology
  - Ellman assay
  - GST Pull-Down Assay
  - Analytical ultracentrifugation
- QUANTIFICATION AND STSTISTICAL ANALYSIS
- DATA AND SOFTWARE AVAILABILITY

SUPPLEMENTAL INFORMATION

Supplemental Information includes seven figures and one table and can be found with this article online at https://doi.org/10.1016/j.celrep.2019.01.097.

AUTHOR CONTRIBUTIONS

Z.J., Z.Y., and Z.L. performed all biochemical and structural experiments. H.L., X.H., X.K., and S.M. performed functional experiments in cultures and in mice. All authors analyzed data and contributed to the writing. Y.L. and M.Z. designed, supervised, and coordinated the research.

DECLARATION OF INTERESTS

The authors declare no competing interests.

REFERENCES

Adams, P.D., Grosse-Kunstleve, R.W., Hung, L.W., Ioerger, T.R., McCoy, A.J., Moriarty, N.W., Read, R.J., Sacchettini, J.C., Sauter, N.K., and Terwilliger, T.C. (2002). PHENIX: building new software for automated crystallographic structure determination. Acta Crystallogr. D Biol. Crystallogr. *58*, 1948–1954.

Almeida, O.P., Schwab, S.G., Lautenschlager, N.T., Morar, B., Greenop, K.R., Flicker, L., and Wildenauer, D. (2008). KIBRA genetic polymorphism influences episodic memory in later life, but does not increase the risk of mild cognitive impairment. J. Cell. Mol. Med. *12 (5A)*, 1672–1676.

Aragón, E., Goerner, N., Zaromytidou, A.I., Xi, Q., Escobedo, A., Massagué, J., and Macias, M.J. (2011). A Smad action turnover switch operated by WW domain readers of a phosphoserine code. Genes Dev. *25*, 1275–1288.

Araki, Y., Zeng, M., Zhang, M., and Huganir, R.L. (2015). Rapid dispersion of SynGAP from synaptic spines triggers AMPA receptor insertion and spine enlargement during LTP. Neuron *85*, 173–189.

Asanuma, K., Campbell, K.N., Kim, K., Faul, C., and Mundel, P. (2007). Nuclear relocation of the nephrin and CD2AP-binding protein dendrin promotes apoptosis of podocytes. Proc. Natl. Acad. Sci. U S A *104*, 10134–10139.

Asanuma, K., Akiba-Takagi, M., Kodama, F., Asao, R., Nagai, Y., Lydia, A., Fukuda, H., Tanaka, E., Shibata, T., Takahara, H., et al. (2011). Dendrin location in podocytes is associated with disease progression in animal and human glomerulopathy. Am. J. Nephrol. *33*, 537–549.

Baumgartner, R., Poernbacher, I., Buser, N., Hafen, E., and Stocker, H. (2010). The WW domain protein Kibra acts upstream of Hippo in Drosophila. Dev. Cell *18*, 309–316.

Bliss, T.V., and Collingridge, G.L. (1993). A synaptic model of memory: long-term potentiation in the hippocampus. Nature *361*, 31–39.

Chen, V.B., Arendall, W.B., 3rd, Headd, J.J., Keedy, D.A., Immormino, R.M., Kapral, G.J., Murray, L.W., Richardson, J.S., and Richardson, D.C. (2010). MolProbity: all-atom structure validation for macromolecular crystallography. Acta Crystallogr. D Biol. Crystallogr. *66*, 12–21.

Chong, P.A., Lin, H., Wrana, J.L., and Forman-Kay, J.D. (2010). Coupling of tandem Smad ubiquitination regulatory factor (Smurf) WW domains modulates target specificity. Proc. Natl. Acad. Sci. U S A *107*, 18404–18409.

Delaglio, F., Grzesiek, S., Vuister, G.W., Zhu, G., Pfeifer, J., and Bax, A. (1995). NMRPipe: a multidimensional spectral processing system based on UNIX pipes. J. Biomol. NMR *6*, 277–293.

Dunér, F., Patrakka, J., Xiao, Z., Larsson, J., Vlamis-Gardikas, A., Pettersson, E., Tryggvason, K., Hultenby, K., and Wernerson, A. (2008). Dendrin expression in glomerulogenesis and in human minimal change nephrotic syndrome. Nephrol. Dial. Transplant. *23*, 2504–2511.

Duning, K., Schurek, E.M., Schlüter, M., Bayer, M., Reinhardt, H.C., Schwab, A., Schaefer, L., Benzing, T., Schermer, B., Saleem, M.A., et al. (2008). KIBRA modulates directional migration of podocytes. J. Am. Soc. Nephrol. *19*, 1891–1903.

Elvira, G., Wasiak, S., Blandford, V., Tong, X.-K., Serrano, A., Fan, X., del Rayo Sánchez-Carbente, M., Servant, F., Bell, A.W., Boismenu, D., et al. (2006). Characterization of an RNA granule from developing brain. Mol. Cell. Proteomics *5*, 635–651.

Emsley, P., and Cowtan, K. (2004). Coot: model-building tools for molecular graphics. Acta Crystallogr. D Biol. Crystallogr. *60*, 2126–2132.

Galecki, P., Szemraj, J., Florkowski, A., Talarowska, M., Bienkiewicz, M., Galecka, E., and Lewinski, A. (2010). Single nucleotide polymorphism of the KIBRA gene in recurrent depressive disorders. Neuroendocrinol. Lett. *31*, 97–102.

Genevet, A., Wehr, M.C., Brain, R., Thompson, B.J., and Tapon, N. (2010). Kibra is a regulator of the Salvador/Warts/Hippo signaling network. Dev. Cell *18*, 300–308.

Heitz, F.D., Farinelli, M., Mohanna, S., Kahn, M., Duning, K., Frey, M.C., Pavenstädt, H., and Mansuy, I.M. (2016). The memory gene KIBRA is a bidirectional regulator of synaptic and structural plasticity in the adult brain. Neurobiol. Learn. Mem. *135*, 100–114.

Herb, A., Wisden, W., Catania, M.V., Maréchal, D., Dresse, A., and Seeburg, P.H. (1997). Prominent dendritic localization in forebrain neurons of a novel mRNA and its product, dendrin. Mol. Cell. Neurosci. *8*, 367–374.

Kato, Y., Ito, M., Kawai, K., Nagata, K., and Tanokura, M. (2002). Determinants of ligand specificity in groups I and IV WW domains as studied by surface plasmon resonance and model building. J. Biol. Chem. *277*, 10173–10177.

Kato, Y., Nagata, K., Takahashi, M., Lian, L., Herrero, J.J., Sudol, M., and Tanokura, M. (2004). Common mechanism of ligand recognition by group II/III WW domains: redefining their functional classification. J. Biol. Chem. *279*, 31833–31841.

Kremerskothen, J., Plaas, C., Büther, K., Finger, I., Veltel, S., Matanis, T., Liedtke, T., and Barnekow, A. (2003). Characterization of KIBRA, a novel WW domain-containing protein. Biochem. Biophys. Res. Commun. *300*, 862–867.

Li, Q., Yang, W., Wang, Y., and Liu, W. (2018). Biochemical and structural studies of the interaction between ARAP1 and CIN85. Biochemistry *57*, 2132–2139.

Macias, M.J., Hyvönen, M., Baraldi, E., Schultz, J., Sudol, M., Saraste, M., and Oschkinat, H. (1996). Structure of the WW domain of a kinase-associated protein complexed with a proline-rich peptide. Nature *382*, 646–649.

Makuch, L., Volk, L., Anggono, V., Johnson, R.C., Yu, Y., Duning, K., Kremerskothen, J., Xia, J., Takamiya, K., and Huganir, R.L. (2011). Regulation of AMPA receptor function by the human memory-associated gene KIBRA. Neuron *71*, 1022–1029.

McCoy, A.J., Grosse-Kunstleve, R.W., Adams, P.D., Winn, M.D., Storoni, L.C., and Read, R.J. (2007). Phaser crystallographic software. J. Appl. Cryst. *40*, 658–674.

Minor, W., Cymborowski, M., Otwinowski, Z., and Chruszcz, M. (2006). HKL-3000: the integration of data reduction and structure solution—from diffraction images to an initial model in minutes. Acta Crystallogr. D Biol. Crystallogr. *62*, 859–866.

Neuner-Jehle, M., Denizot, J.P., Borbély, A.A., and Mallet, J. (1996). Characterization and sleep deprivation-induced expression modulation of Dendrin, a novel dendritic protein in rat brain neurons. J. Neurosci. Res. *46*, 138–151.

Papassotiropoulos, A., Stephan, D.A., Huentelman, M.J., Hoerndli, F.J., Craig, D.W., Pearson, J.V., Huynh, K.D., Brunner, F., Corneveaux, J., Osborne, D., et al. (2006). Common Kibra alleles are associated with human memory performance. Science *314*, 475–478.

Patrakka, J., Xiao, Z., Nukui, M., Takemoto, M., He, L., Oddsson, A., Perisic, L., Kaukinen, A., Szigyarto, C.A., Uhlén, M., et al. (2007). Expression and subcellular distribution of novel glomerulus-associated proteins dendrin, ehd3, sh2d4a, plekhh2, and 2310066E14Rik. J. Am. Soc. Nephrol. *18*, 689–697.

Rodríguez-Rodríguez, E., Infante, J., Llorca, J., Mateo, I., Sánchez-Quintana, C., García-Gorostiaga, I., Sánchez-Juan, P., Berciano, J., and Combarros, O. (2009). Age-dependent association of KIBRA genetic variation and Alzheimer's disease risk. Neurobiol. Aging *30*, 322–324.

Schleinkofer, K., Wiedemann, U., Otte, L., Wang, T., Krause, G., Oschkinat, H., and Wade, R.C. (2004). Comparative structural and energetic analysis of WW domain-peptide interactions. J. Mol. Biol. *344*, 865–881.

Schuck, P. (2000). Size-distribution analysis of macromolecules by sedimentation velocity ultracentrifugation and lamm equation modeling. Biophys. J. *78*, 1606–1619.

Talarowska, M., Szemraj, J., Kowalczyk, M., and Gałecki, P. (2016). Serum KIBRA mRNA and protein expression and cognitive functions in depression. Med. Sci. Monit. *22*, 152–160.

Tracy, T.E., Sohn, P.D., Minami, S.S., Wang, C., Min, S.W., Li, Y., Zhou, Y., Le, D., Lo, I., Ponnusamy, R., et al. (2016). Acetylated tau obstructs KIBRA-mediated signaling in synaptic plasticity and promotes tauopathy-related memory loss. Neuron *90*, 245–260.

Tu, W., Xu, X., Peng, L., Zhong, X., Zhang, W., Soundarapandian, M.M., Balel, C., Wang, M., Jia, N., Zhang, W., et al. (2010). DAPK1 interaction with NMDA receptor NR2B subunits mediates brain damage in stroke. Cell *140*, 222–234.

Vogt-Eisele, A., Krüger, C., Duning, K., Weber, D., Spoelgen, R., Pitzer, C., Plaas, C., Eisenhardt, G., Meyer, A., Vogt, G., et al. (2014). KIBRA (KIdney/BRAin protein) regulates learning and memory and stabilizes Protein kinase Mζ. J. Neurochem. *128*, 686–700.

Vranken, W.F., Boucher, W., Stevens, T.J., Fogh, R.H., Pajon, A., Llinas, M., Ulrich, E.L., Markley, J.L., Ionides, J., and Laue, E.D. (2005). The CCPN data model for NMR spectroscopy: development of a software pipeline. Proteins *59*, 687–696.

Weins, A., Wong, J.S., Basgen, J.M., Gupta, R., Daehn, I., Casagrande, L., Lessman, D., Schwartzman, M., Meliambro, K., Patrakka, J., et al. (2015).

Dendrin ablation prolongs life span by delaying kidney failure. Am. J. Pathol. *185*, 2143–2157.

Willsey, A.J., Fernandez, T.V., Yu, D., King, R.A., Dietrich, A., Xing, J., Sanders, S.J., Mandell, J.D., Huang, A.Y., Richer, P., et al. (2017). De novo coding variants are strongly associated with Tourette disorder. Neuron *94*, 486–499.e9.

Xu, J., and Xia, J. (2006–2007). Structure and function of PICK1. Neurosignals *15*, 190–201.

Yang, X., Yao, C., Tian, T., Li, X., Yan, H., Wu, J., Li, H., Pei, L., Liu, D., Tian, Q., et al. (2018). A novel mechanism of memory loss in Alzheimer's disease mice via the degeneration of entorhinal-CA1 synapses. Mol. Psychiatry *23*, 199–210.

Yoshihama, Y., Sasaki, K., Horikoshi, Y., Suzuki, A., Ohtsuka, T., Hakuno, F., Takahashi, S., Ohno, S., and Chida, K. (2011). KIBRA suppresses apical exocytosis through inhibition of aPKC kinase activity in epithelial cells. Curr. Biol. *21*, 705–711.

Yu, J., Zheng, Y., Dong, J., Klusza, S., Deng, W.M., and Pan, D. (2010). Kibra functions as a tumor suppressor protein that regulates Hippo signaling in conjunction with Merlin and Expanded. Dev. Cell *18*, 288–299.

Zhang, H., Kranzler, H.R., Poling, J., Gruen, J.R., and Gelernter, J. (2009). Cognitive flexibility is associated with KIBRA variant and modulated by recent tobacco use. Neuropsychopharmacology *34*, 2508–2516.

Zhao, H., Piszczek, G., and Schuck, P. (2015). SEDPHAT—a platform for global ITC analysis and global multi-method analysis of molecular interactions. Methods *76*, 137–148.

Zhu, J., Zhou, Q., Shang, Y., Li, H., Peng, M., Ke, X., Weng, Z., Zhang, R., Huang, X., Li, S.S.C., et al. (2017). Synaptic Targeting and Function of SAPAPs Mediated by Phosphorylation-Dependent Binding to PSD-95 MAGUKs. Cell Rep. *21*, 3781–3793.

STAR★METHODS

KEY RESOURCES TABLE

REAGENT or RESOURCE	SOURCE	IDENTIFIER
Antibodies		
Goat polyclonal anti-GFP	Abcam	Cat#ab6658 RRID:AB_305631
Rabbit polyclonal anti-Kibra	Sigma	Cat#HPA038016
Mouse monoclonal anti-GluR1	Synaptic System	Cat#182 011
Rabbit polyclonal anti-GluR1	Synaptic System	Cat#182 003
Rabbit polyclonal anti-GluR2	Synaptic System	Cat#182 103
Mouse monoclonal anti-NR1	Synaptic System	Cat#114 011
Mouse monoclonal anti-PSD95	Synaptic System	Cat#124 011BT
Rabbit polyclonal anti-Dendrin	abcam	Cat#ab204787
Mouse monoclonal anti-beta Actin	Proteintech	Cat# 66009-1-Ig
Rabbit polyclonal anti-NR2B	Millipore	Cat#AB1557
Rabbit monoclonal anti-NR2A	abcam	Cat#ab124913
Chicken polyclonal anti-MAP2	abcam	Cat#ab5392
Mouse monoclonal anti-PKC1	Millipore	Cat#05-154
Rabbit polyclonal anti-PKM	Santa Cruz	Cat#sc-292640
Donkey anti-Mouse IgG Secondary Antibody, Alexa Fluor 546	Invitrogen	Cat#A-10036
Goat anti-Chicken IgY Secondary Antibody,Alexa Fluor 488	Invitrogen	Cat#A-10039
Goat anti-Chicken IgY Secondary Antibody, Alexa Fluor 647	Invitrogen	Cat#A-21449
Donkey anti-Rabbit IgG Secondary Antibody, Alexa Fluor 546	Invitrogen	Cat#A10040
Donkey anti-Rabbit IgG Secondary Antibody, Alexa Fluor 488	Invitrogen	Cat#A-21206
Donkey anti-Goat IgG Secondary Anitobody, HRP	Invitrogen	Cat#A16005
Bacterial and Virus Strains		
Escherichia coli: BL21 (DE3)	Invitrogen	Cat#C600003
AAV-CAG-eGFP	Genechem	N/A
AAV-CAG-P_C-eGFP	Genechem	N/A
AAV-CAG-P_B-eGFP	Genechem	N/A
Lenti-U6-ssiDDN-eGFP	Genechem	N/A
Lenti-U6-siDDN-eGFP	Genechem	N/A
Chemicals, Peptides, and Recombinant Proteins		
Synthesized Dendrin PY23CT peptide (DRPPPYVAPPSY EGPHRTLGTKRGP)	China Peptides	N/A
Synthesized Dendrin PY23 peptide (DRPPPYVAPPSY EGPHR)	China Peptides	N/A
Synthesized DN1A peptide (DRPPPYAPPSYEG)	China Peptides	N/A
Synthesized DN2A peptide (DRPPPYAAPPSYEG)	China Peptides	N/A
Synthesized DN3A peptide (DRPPPYAAAPPSYEG)	China Peptides	N/A
Synthesized DN4A peptide (DRPPPYAAAAPPSYEG)	China Peptides	N/A
Synthesized DN5A peptide (DRPPPYAAAAAPPSYEG)	China Peptides	N/A
Synthesized DN2G peptide (DRPPPYGGPPSYEG)	China Peptides	N/A
Synthesized P_C' peptide (GRKKRRQRRRGDRPPPAR PPPSAEGPHRTLG)	SciLight Biotechnology	N/A

REAGENT or RESOURCE	SOURCE	IDENTIFIER
Synthesized P_B' peptide (GRKKRRQRRRGDRPPPYR PPPSYEGPHRTLG)	SciLight Biotechnology	N/A
Recombinant protein: Kibra WW12 (aa E5-K97, Uniprot: Q5SXA9)	This paper	N/A
Recombinant protein: Kibra WW1 (aa E5-K43, Uniprot: Q5SXA9)	This paper	N/A
Recombinant protein: Kibra WW2 (aa K43-K97, Uniprot: Q5SXA9)	This paper	N/A
Recombinant protein: Kibra WW12 (crystallization, aa E5-H132, Uniprot: Q5SXA9)	This paper	N/A
Recombinant protein: WWC2 WW12 (aa Q9-K101, Uniprot: Q6NXJ0)	This paper	N/A
Recombinant protein: YAP WW12 (aa E151-R251, Uniprot: P46938)	This paper	N/A
Recombinant protein: ITCH WW12 (aa A287-L352, Uniprot: Q8C863)	This paper	N/A
Recombinant protein: ITCH WW34 (aa G399-T472, Uniprot Q8C863)	This paper	N/A
Recombinant protein: Dendrin PY123CT (aa G191-R250, Uniprot: Q80TS7)	This paper	N/A
Recombinant protein: Dendrin PY23CT (aa A216-R250, Uniprot: Q80TS7)	This paper	N/A
Recombinant protein: Dendrin PY1 (aa G191-A216, Uniprot: Q80TS7)	This paper	N/A
Recombinant protein: Dendrin PY23 (aa P217-G235, Uniprot: Q80TS7)	This paper	N/A
Recombinant protein: PATJ PDZ8-10 (aa L1421-D1801, Uniprot: Q8NI35)	This paper	N/A
Recombinant protein: CIN85 SH3B (aa G96-D160, Uniprot: Q8R550)	Li et al., 2018	N/A
poly-D-lysine	Sigma	Cat#27964-99-4
Hoechst 33342	Invitrogen	Cat#H1399
Neurobasal medium	GIBCO	Cat#21103-049
GlutaMax	GIBCO	Cat#35050-061
B27	Sigma	Cat#17504-044
HBSS basic (1X)	GIBCO	Cat#C14175500BT
DMEM/F-12(1:1) basic (1X)	GIBCO	Cat#C11330500BT
Pen Strep	GIBCO	Cat#15140-122
Pro ES	Sera Pro	Cat#S742S-500
0.25% Trypsin (1X)	GIBCO	Cat#15050-065
Isoflurane	RWD	Cat#R510-22
Potassium D-gluconate	Sigma	Cat#G4500
CNQX	Tocris	Cat#1645
D-AP5	Tocris	Cat#0106
Bicuculline	EN2D	Cat#EA109-0050
TTX	Tocris	Cat#4368
$C_6H_{12}O_6$ (D-(+)-Glucose)	Sigma	Cat#G7021
CsCl	Sigma	Cat#746487
Protease Inhibitor	Thermo SCIENTIFIC	Cat#78425

(*Continued on next page*)

REAGENT or RESOURCE	SOURCE	IDENTIFIER
Critical Commercial Assays		
Viafect transfection kit	Promega	Cat#E4981
BCA Protein Assay Kit	Thermo SCIENTIFIC	Cat#23227
Deposited Data		
Kibra WW12/Dendrin PY23CT complex structure	This paper	PDB: 6J69
Experimental Models: Cell Lines		
Human: HeLa cells	ATCC	CCL-2
Human: HEK293T cells	ATCC	CRL-3216
Mouse: embryonic day 18 hippocampal primary cultured neuron	N/A	N/A
Experimental Models: Organisms/Strains		
Mouse: C57BL/6	NBRI	N000013
Recombinant DNA		
Plasmid: mCherry-Kibra (full length, Uniprot: Q8IX03)	This paper	N/A
Plasmid: GFP-Dendrin (full length, Uniprot: Q80TS7)	This paper	N/A
Plasmid: GFP-P_B (aa D222-G241, Uniprot: Q80TS7)	This paper	N/A
Plasmid: GFP-P_C (aa D222-G241 Y227/233A, Uniprot: Q80TS7)	This paper	N/A
Plasmid: GFP-DN1A (aa P217-G245 delete V228, Uniprot: Q80TS7)	This paper	N/A
Plasmid: GFP-Kibra (full length, Uniprot: Q8IX03)	This paper	N/A
Software and Algorithms		
Origin	OriginLab	http://www.originlab.com/
HKL3000	Minor et al., 2006	http://www.hkl-xray.com/
PHASER	McCoy et al., 2007	https://www.phenix-online.org/
Phenix	Adams et al., 2002	https://www.phenix-online.org/
Coot	Emsley and Cowtan, 2004	http://www2.mrc-lmb.cam.ac.uk/personal/pemsley/coot/
NMRPipe	Delaglio et al., 1995	https://spin.niddk.nih.gov/bax/software/NMRPipe/
Sparky	T. D. Goddard and D. G. Kneller, SPARKY, University of California, San Francisco	https://www.cgl.ucsf.edu/home/sparky/
CCPN	Vranken et al., 2005	https://www.ccpn.ac.uk/
PyMOL	PyMOL	http://pymol.sourceforge.net/
ASTRA6	Wyatt	http://www.wyatt.com/products/software/astra.html
ImageJ	NIH	https://imagej.nih.gov/ij/
GraphPad Prism	GraphPad Software Inc	http://www.graphpad.com/scientific-software/prism/
[WMT-100]	Tai Meng Technology Co., Ltd	https://www.tme.com.cn
Clampfit	Molecular Devices	https://www.moleculardevices.com.cn
Med64 Mobius	Alpha MED Scientific	https://www.med64.com
Sigmaplot	SYSTAT	https://www.systatsoftware.com
ZEN	Zeiss	https://www.zeiss.com
MolProbity	Chen et al., 2010	http://molprobity.biochem.duke.edu/
SEDFIT	Schuck, 2000	http://www.analyticalultracentrifugation.com/
SEDPHAT	Zhao et al., 2015	http://www.analyticalultracentrifugation.com/

CONTACT FOR REAGENT AND RESOURCE SHARING

Further information and requests for resources and reagents should be directed to and will be fulfilled by the Lead Contact, Mingjie Zhang (mzhang@ust.hk).

EXPERIMENTAL MODEL AND SUBJECT DETAILS

HeLa Cells and HEK293T Cells Culture

HeLa and HEK293K cells (both from ATCC) were cultured in DMEM media supported by fetal bovine serum. Cells were tested negative for mycoplasma contamination by cytoplasmic DAPI staining, and these cells were not further individually authenticated.

Primary Neuronal Culture

Primary hippocampal neuron cultures were prepared from the E18 C57BL/6 WT mice for imaging and dendritic spine analysis, as described before (Yang et al., 2018). Cells were seeded on coverslips coated by 100 μg/mL poly-D-lysine (27964-99-4, Sigma) in 24-well plates. Cells were incubated at 37°C in a humidified atmosphere of 95% O2/5% CO2 at CO2 INCUBATOR (HF90, Heal Force). Cultures were maintained for 15-18 days *in vitro* in fresh serum free Neurobasal medium (21103-049, GIBCO) supported by 1 × GlutaMax(35050-061, GIBCO)and 1 × B27 (17504-044, Sigma) supplement and fed every 3 days with fresh media without GlutaMax.

Animals

All mice (C57BL/6) used in this study were bred and fed in the same conditions in accordance with institutional guidelines of the Animal Care and Use Committee (Huazhong University of Science and Technology, Wuhan, China) within the University's animal care facility. Mice were housed in groups of three to five per cage under a 12 h light-dark cycle, with lights on at 8:00 am, at a consistent ambient temperature (21 $\pm$ 1°C) and humidity (50 $\pm$ 5%). In the present study, only male mice were used to avoid behavioral variability between genders. All experiments and analyses were performed blind to the mice genotype or treatment.

METHOD DETAILS

Plasmid Construction, Protein Expression and Purification

For protein expression, the coding regions of genes for desired proteins were individually cloned into a pET vector and recombinant proteins were expressed in Codon-plus BL21 (DE3) *Escherichia coli* cells. All recombinant proteins were purified using Ni^{2+}-nitrilotri-acetic acid agarose (Ni-NTA) column followed by size-exclusion chromatography in general buffer containing 50 mM Tris-HCl (pH 7.8), 100 mM NaCl, 1 mM EDTA and 1 mM DTT (no DTT was added for purifying oxidized W88C-Kibra WW12). All tags of recombinant proteins were removed before X-ray crystallography and NMR experiments, except for ^{15}N-lablled Trx-WW2. All peptides were commercially synthesized (China Peptides for ITC, NMR and crystallization; SciLight Biotechnology, Beijing, China for neuronal culture studies).

Isothermal Titration Calorimetry Assay

Isothermal Titration Calorimetry (ITC) experiments were performed on a VP-ITC calorimeter (MicroCal) at 25°C. Titration buffer contained 50 mM Tris-HCl (pH 7.8), 100 mM NaCl, 1 mM EDTA and 1 mM DTT (except for 5 mM DTT to maintain W88C-Kibra WW12 in the reduced form and no DTT to maintain W88C-Kibra WW12 in the oxidized form). For a typical experiment, each titration point was performed by injecting a 10 μL aliquot of protein sample (100 μM) into the cell containing another reactant (10 μM) at a time interval of 120 s to ensure that the titration peak returned to the baseline. For the competition experiments, proteins in the syringe were titrated to a mixture with a 2-fold molar concentration excess of the competitor over the reactants in the cell. The titration data were analyzed using one-site binding or competitive binding model by Origin7.0 (MicroCal).

Analytical Gel Filtration Chromatography Coupled with Static Light Scattering

An AKTA FPLC system (GE Healthcare) equipped with analytical gel filtration column and coupled with static light scattering and differential refractive index detector (miniDawn, Wyatt) was used for the assays. Protein samples (100 μL with concentration of 100 μM) were loaded to a Superose 12 10/300 GL column (GE Healthcare) pre-equilibrated with assay buffer (same with ITC). Data were analyzed with ASTRA6 (Wyatt).

Crystallography

Kibra (residues 5-132)/Dendrin PY23CT peptide (residues 222-246) complex crystal was obtained by hanging drop vapor diffusion method at 4°C within 3-5 days. To set up a hanging drop, 1 μL of concentrated protein mixture (10~20 mg/mL) at 1:1 stoichiometric ratio was mixed with 1 μL of crystallization solution containing 0.4 M sodium citrate, 0.1 M HEPES pH 7.5, 16% 2-Propanol, and then equilibrated against 400 μL of reservoir solution. All diffraction data were collected at the Shanghai Synchrotron Radiation Facility. Data were processed and scaled using HKL3000 (Minor et al., 2006).

The initial phase of Kibra/Dendrin complex was determined by the program PHASER using the structure of Kibra/Lats1 complex (unpublished) as the searching model (McCoy et al., 2007). The Kibra WW12 tandem structure and Dendrin PY tandem structure were built manually based on the $2F_{obs}$-F_{calc} and F_{obs}-F_{calc} difference Fourier maps. Structural model refinement was carried out using Phenix refinement (Adams et al., 2002). Coot was used for manual model building and modifications (Emsley and Cowtan, 2004). Detailed data collection and refinement statistics are summarized in Table S1. All structure figures were prepared using PyMOL (http://pymol.sourceforge.net/).

NMR Experiments

NMR samples were dissolved in 100 mM phosphate buffer (Na_2HPO_4-NaH_2PO_4, 1 mM DTT and 1 mM EDTA, pH 6.5) with 90% H_2O/ 10% D_2O, except that W88C-Kibra WW12 was dissolved in the same buffer with 5 mM DTT. The concentrations of proteins in NMR studies were 0.2 mM for the ^{15}N-HSQC spectra and 1.0 mM for ^{15}N-NOESY, HNCACB, CACB(CO)NH and ^1H-^{15}N heteronuclear NOE experiments. NMR spectra were acquired on Varian Inova 750 or 800 MHz spectrometers at 30°C. NMR data were processed using NMRPipe (Delaglio et al., 1995) and analyzed using Sparky (T. D. Goddard and D. G. Kneller, SPARKY 3, University of California, San Francisco) and CCPN (Vranken et al., 2005). Backbone resonance assignment of Kibra WW12 tandem in complex with unlabeled Dendrin PY23CT were obtained via the standard heteronuclear triple resonance correlation experiments using ^{15}N, ^{13}C-double labeled WW12.

Cell Cultures and Imaging

For each well in a 12-well plate, plasmids (0.5 μg) expressing mCherry-Kibra and GFP-tagged Dendrin peptide were co-transfected in HeLa cells using Viafect (Promega, Madison, WI). Cells were fixed with 4% paraformaldehyde (PFA) 24 h after transfection. Fixed cells were imaged using Zeiss LSM 880 confocal microscope by a 63x oil objective. DAPI staining was used to define nuclear localization of cells. Images were processed and analyzed using ImageJ software (https://imagej.nih.gov/ij/).

After 16 days (DIV 16), peptides were performed by exposure of primary hippocampal neuron cultures to 5 μM for 48 h. Control cultures were of no peptide treatment and processed in parallel. Cells were fixed at DIV18 with 4% PFA for immunofluorescent and then mounted on slides for imagine. Neuronal images were acquired on LSM 800 microscope (Zeiss) with a 63x oil-immersion lens. For quantification, we selected all spines on a secondary dendrite branching immediately after a primary dendrite as described previously (Araki et al., 2015). For a whole CA1 pyramidal cell imaging, we used z stack and tile-scan of LSM 800 microscope. ImageJ software was used for calculating the cell size.

Stereotaxic Injection

Mice (C57BL/6 6 weeks for electrophysiological experiment, 10 weeks for behavior and protein qualification experiments, male) were anaesthetized with isoflurane (2%–5%, RWD) and placed in a stereotaxic apparatus, with head fixed and skull exposed. Burr holes were made and a micro syringe (World Precision Instruments) was slowly lowered into the dorsal CA1 at 2.06 mm anteroposterior, 1.38 mm mediolateral and 1.60 mm dorsoventral relative to bregma. Virus (Genechem) expressing desired peptides/siRNA (1 μL) was pressure-injected into each hemisphere, as described before (Zhu et al., 2017; Li et al., 2018). Before suture, the syringe was kept still for 5 min and then slowly retracted. The mice were placed on a heating pad throughout the duration of the surgery and recovery from anesthesia. The electrophysiological and behavior experiments were proceeded 4 weeks after the virus injection.

Western Blots and Staining

Hippocampus isolated from the mouse brains were homogenized in ice-cold lysis buffer containing 50 mM Tris-HCl, 150 mM NaCl, 1% NP-40, 2 mM EDTA, 1 mM Na-orthovanadate, (pH 7.4), and proteinase inhibitor mixture (Thermo SCIENTIFIC, 1 mL/10 g tissue) and collected the homogenate to centrifuge at 1,000 g at 4°C for 10 min. After that, the suspension was separated into precipitation rich of nucleoproteins and supernatant S1 which was further centrifuged at 12,000 g at 4°C for 20 min to separate precipitation P2 (CM) and supernatant S2. Then P2 (CM) was suspended with 100 mL HEPES (4 mM).

The total cell lysates and the CM fraction were added to one-third volume of 4 × sample buffer and boiled for 10 min in a water bath. Protein concentration in the extracts was determined by BCA Protein Assay Kit (Thermo SCIENTIFIC). Proteins were separated by 10% sodium dodecyl sulfate polyacrylamide gels (SDS-PAGE), and were transferred onto nitrocellulose membranes. Membranes were then incubated with blocking solution (5% nonfat dried milk) for 30 min at room temperature, washed three times, and incubated with primary antibody against Kibra (1:1000, Sigma HPA038016), GluR1 (1:1000, Synaptic System 182 011), GluR2 (1:1000, Synaptic System 182 103), NR1 (1:1000, Synaptic System 114 011), NR2A (1:1000, Millipore AB1555P), NR2B (1:1000, Abcam ab81271), PSD95 (1:1000; Synaptic System 124 003), Dendrin (1:1000, Abcam ab204787), or beta actin (1:2000, proteintech 66009-1-lg) for 2 h at room temperature. Membranes were washed three times with TBST buffer and incubated with the appropriate secondary antibodies (1:1000 dilution) for 1 h followed by washing for four times, and then the protein signals were scanned using an Infrared Imaging System (Odyssey, LI-COR).

After fixation with 4% PFA in PBS, the cells were incubated with anti-Kibra (1:200, Sigma HPA038016), or anti-MAP2 (1:8000, Abcam ab5392), or anti-PSD95 (1:300, Synaptic Systems 124 003), or anti-GluA (1:300, Synaptic System 182 411) antibodies overnight. The cells were then washed with PBS and incubated with Alexa 488-, 594-, 647-conjugated secondary antibodies

(1:200, Invitrogen) for 60-90 min. To label the nucleus, cells were also incubated with Hoechst (1:1500, Invitrogen) for 5 min. A laser-scanning confocal microscope (LSM 800; Zeiss) was used for fluorescence imaging.

Morris Water Maze Tests

The water maze task consists a circular tank (120 cm-diameter) filled with opaque water (21-23°C) and a hidden platform (6 cm-diameter) submerged 1 cm below the surface of the water, as described previously (Tu et al., 2010). The device with matching software [WMT-100] was purchased from Tai Meng Technology Co., Ltd (Chengdu, China). Before the start of training trials, the mice were allowed to acclimate to testing room for 30 min. The mice were trained to find the invisible platform within 90 s on 6 consecutive days with 3 trials per day. Mice that failed to find the platform within 90 s, were guided to find the platform and allowed to stay for 15 s. Escape latency to find the hidden platform, path length, and swimming velocity were recorded. After one day of rest, the platform was removed and mice were individually set afloat to search the pool for 90 s (probe tests). Then, the time spent in each quadrant was analyzed.

Electrophysiology

Hippocampal slices (300 μm) were prepared as described previously (Yang et al., 2018). The slices were transferred to a holding chamber that contains artificial cerebrospinal fluid (in mM: 124 NaCl, 3 KCl, 26 NaHCO$_3$, 1.25 NaH$_2$PO$_4$, 1.2 MgCl$_2$, 10 C$_6$H$_{12}$O$_6$, and 2 CaCl$_2$, pH 7.4, 305 mOsm). The slices were allowed to recover at 31.5°C for 30 min and then at room temperature for 1 h. Acute slices were transferred to a recording chamber continuously, which was perfused with oxygenated artificial cerebrospinal fluid (2 mL/min) and maintained at room temperature. For whole-cell patch-clamp recordings from the CA1 pyramidal cells, hippocampal slices were visualized via input resistance-DIC by using an Axioskop 2FS equipped with Hamamatsu C2400-07E optics (Hamamatsu City, Japan). Basic electrophysiological properties were recorded when stable recordings were achieved with good access resistance ($\sim$20 MΩ). The mEPSCs were recorded using an internal solution containing (in mM) 140 potassium gluconate, 10 HEPES, 0.2 EGTA, 2 Mg^{2+}ATP, 2 NaCl, and 0.3 NaGTP and an external solution containing 10 μM bicuculline and 1 μM tetrodotoxin (TTX). The mIPSCs were recorded with an internal solution containing (in mM) 153.3 CsCl, 1 MgCl$_2$, 5 EGTA, 10 HEPES, 4 Mg^{2+}ATP and an external solution containing 10 μM 6-cyano-7-nitroquinoxaline-2,3-dione (CNQX), 50 μM APV, and 1 μM TTX. The data were collected at 10 kHz and filtered with a low-pass filter at 2 kHz. Miniature events were analyzed in Clampfit 10.2 software (Molecular Devices, Sunnyvale, CA, USA) based on the waveforms of the events.

For the induction of LTP, the hippocampal slices (300 μm) were prepared as described above. For field potential recordings, acute hippocampal slices were placed on a Med64-multielectrode array (Alpha MED Scientific). Field Excitatory Post Synaptic Potentials (fEPSP) were elicited and recorded via planar electrodes of the Probe AL-MED-P515A by aligning the electrodes and the stratum radiatum region of hippocampal slices. An input-output curve was performed at the beginning of each recording to determine the appropriate stimulation intensity. Test stimuli at 30%–40% of maximal intensity were delivered at 0.05 Hz and a stable baseline of fEPSP of 30 min was established before LTP induction. The evoked fEPSPs were measured by taking the slope of the rising phase between 10 and 90% of the peak response. LTP was induced using a theta-burst protocol comprised of 3 trains delivered every 10 s, each train containing 10 bursts at 5 Hz, each burst containing four pulses at 100 Hz. LTP was induced at 10 μA above test intensity to ensure robust LTP induction. Recordings lasted for an hour after induction. Recordings and analysis were performed using Med64 Mobius Software (Alpha MED Scientific).

Ellman assay

Kibra WW12W88C was oxidized at room temperature by exposing the sample to air oxygen. The oxidized Kibra WW12W88C could be completely reduced by addition of 5 mM DTT into the air-oxidized protein sample. In Ellman assays, 10 μL of 4 mM DTNB solution, 25 μL of 2 M Tris (pH 8.0), 50 μL of each protein sample, and 915 μL 6 M Guanidine (pH 8.0) were mixed. The absorbance of each reaction mixture at 412 nm was converted into the amount of free -SH for each protein sample. For the DTNB assays of the reduced protein samples, the excess DTT in each sample mixture was removed by passing the protein sample through a PD-10 desalting columns (GE Healthcare).

GST Pull-Down Assay

For each 10 cm dishes, plasmids (8 μg) expressing GFP-Kibra or GFP-Dendrin were transfected in HEK293T cells using Viafect (Promega, Madison, WI). After 20 h of transfection, cells were lysed in an ice-cold cell lysis buffer containing 50 mM HEPES (pH 7.4), 150 mM NaCl, 10% glycerol, 1 mM EGTA, 1% Triton, and protease inhibitor cocktail for 1 h at 4°C, followed by centrifugation at 14,000 rpm for 10 min at 4°C. The supernatant was incubated with 4 nmol GST-tagged PATJ-PDZ8-10 (for GFP-Kibra binding) or GST-tagged CIN85-SH3B (for GFP-Dendrin binding) or GST (as control) with or without addition of peptides (for GFP-Kibra) or purified Kibra WW12 (for GFP-Dendrin) for 1 h at 4°C. An aliquot of 25 μL glutathione Sepharose beads were used to pull down the GFP-tagged proteins in each reaction. After extensive washing, the captured proteins were separated by SDS-PAGE and detected by western blot using anti-GFP antibody (1:5000, Abcam ab6658).

Analytical ultracentrifugation

Analytical ultracentrifugation (AUC) analysis sedimentation experiments were performed on a Beckman XL-I analytical ultracentrifuge equipped with an eight-cell rotor at 25°C. The sedimentation velocity analysis was performed at the speed of 36,000 rpm. 13.5 μM Kibra WW12/Dendrin PY23CT complex sample in assay buffer (same with ITC) was used in sedimentation velocity analysis. The sedimentation velocity data were analyzed and fitted to a continuous sedimentation coefficient distribution model using the program SEDFIT (Schuck, 2000). AUC sedimentation equilibrium analysis was performed using a complex sample at two different concentrations (6 μM & 12 μM). The rotor speed for the sedimentation equilibrium experiment was 16,000 rpm. The data were analyzed and fitted to a species analysis model using the program SEDPHAT (Zhao et al., 2015).

QUANTIFICATION AND STSTISTICAL ANALYSIS

All data represent Mean ± SEM; ns, not significant, *$p < 0.05$, **$p < 0.01$, ***$p < 0.001$ and ****$p < 0.0001$ using unpaired two-tailed Student's t tests (t test). Statistical parameters including the definitions and exact values of 'n' are reported in the corresponding Figure Legends. All statistical analyses were performed using GraphPad Prism. All quantifications were performed by investigators blind to the experimental conditions.

DATA AND SOFTWARE AVAILABILITY

The atomic coordinates of the Kibra WW12/Dendrin PY23CT complex are deposited to the Protein Data Bank under the accession code PDB: 6J69

Supplemental Information

Kibra Modulates Learning

and Memory via Binding to Dendrin

Zeyang Ji, Hao Li, Zhou Yang, Xian Huang, Xiao Ke, Sehui Ma, Zhijie Lin, Youming Lu, and Mingjie Zhang

SUPPLEMENTARY FIGURES AND TABLES
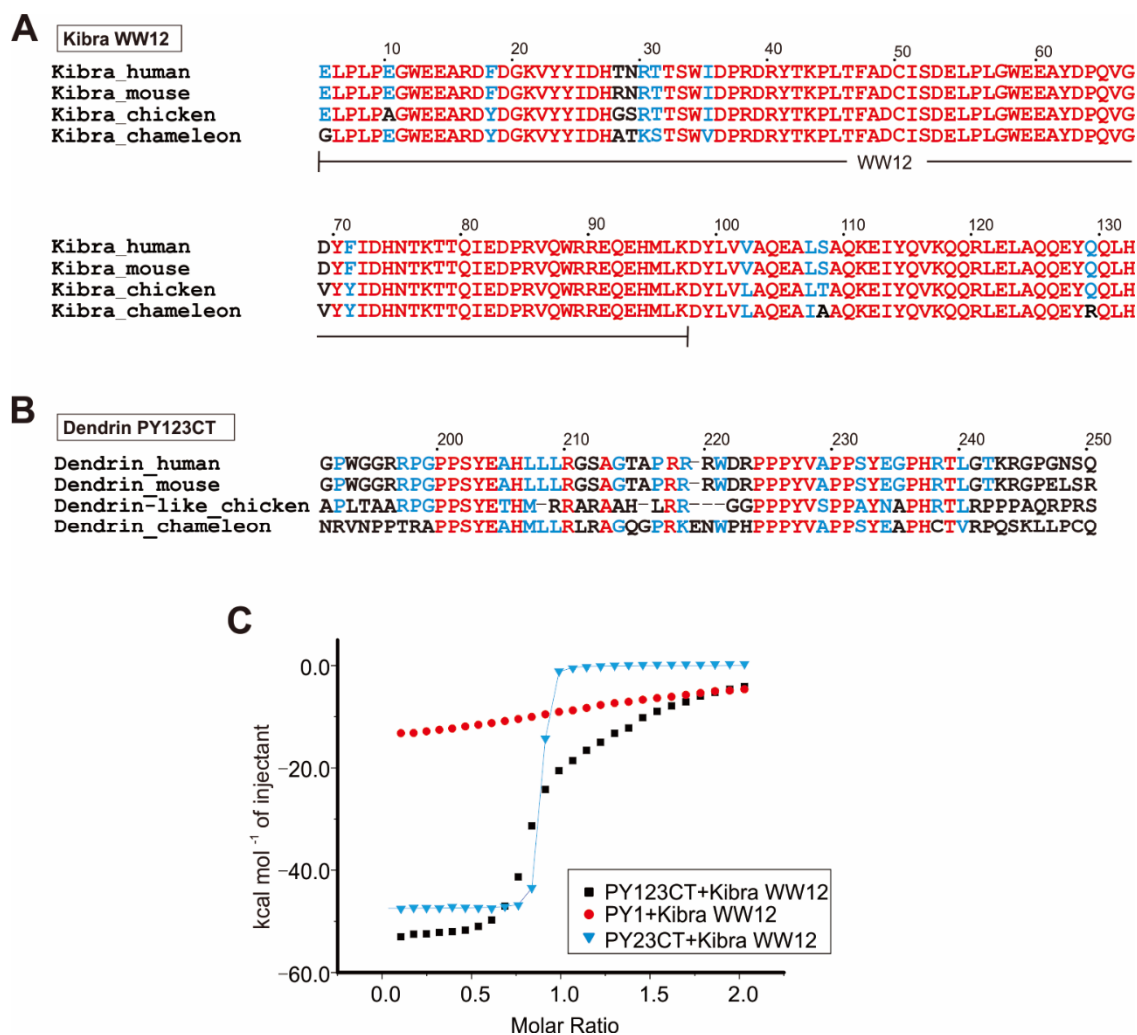
Figure S1: Kibra WW12 Binds to Dendrin PY23CT at A Manner of Super-High Affinity and Specificity. Related to Figure 1.

(A) Amino acid sequence alignment of the WW12 tandem of Kibra from different species. In this alignment totally conserved residues are colored in red and conserved residues are colored in blue.

(B) Sequence alignment of the PY-motifs of Dendrin from different species. In this alignment totally conserved residues are colored in red and conserved residues are colored in blue.

(C) ITC-based measurement of the binding between WW12 and PY123CT, PY1 or PY23CT.

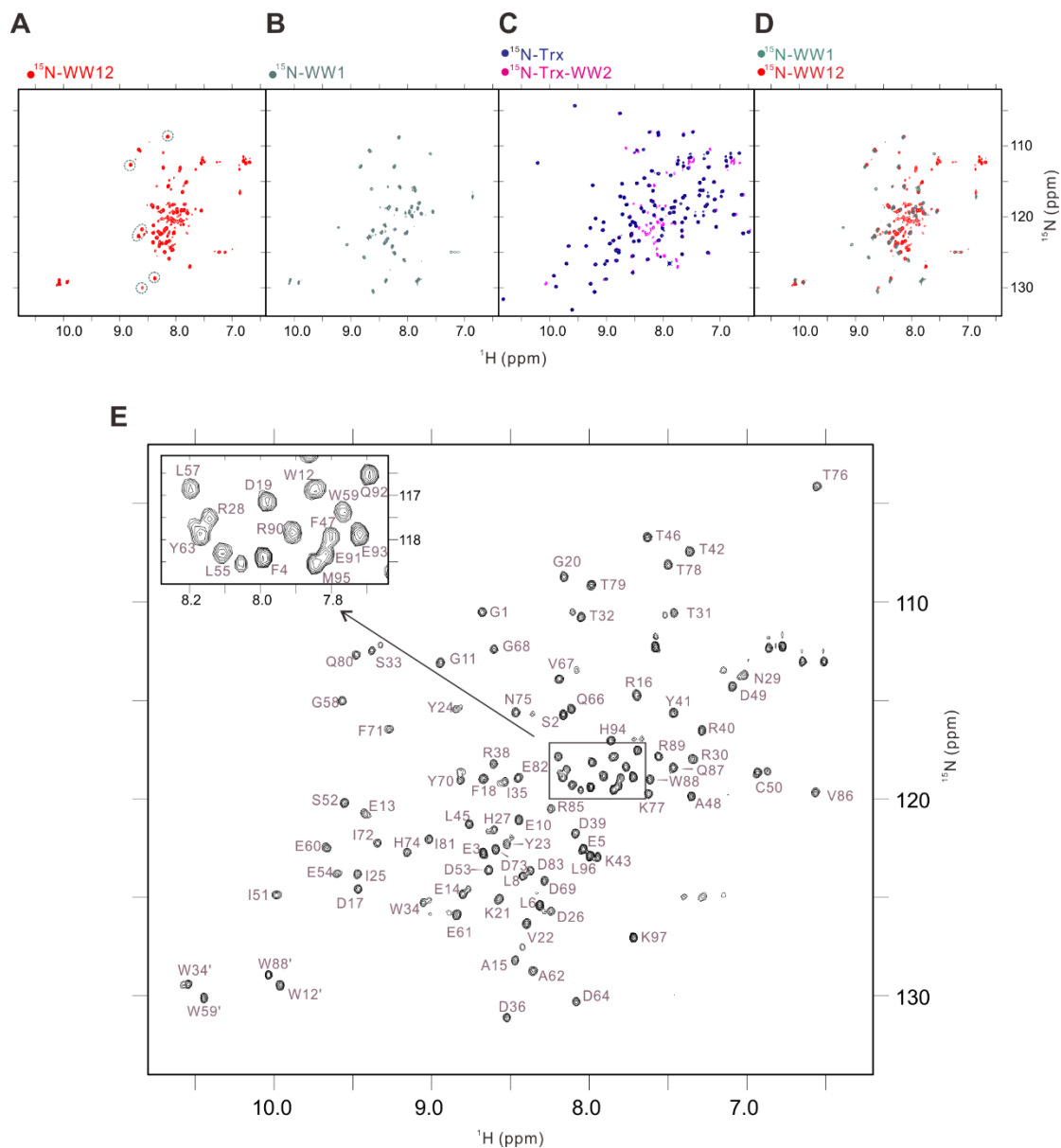**Figure S2. Dendrin PY23CT Binding Induced Kibra WW12 Supramodule Formation. Related to Figure 2.**

(A) ^{15}N-HSQC spectrum of ^{15}N-labeled Kibra WW12. Narrow amide peak chemical shift dispersions of the spectrum indicated that part of Kibra WW12 is not well-folded. Selective peaks from WW1 are highlighted with dotted circles in *teal*.

(B) ^{15}N-HSQC spectrum of ^{15}N-labeled WW1. Well-dispersed amide peaks indicated that the isolated WW1 is folded in solution.

(C) ^{15}N-HSQC spectrum of ^{15}N-labeled Trx-tag (*blue*) overlay with ^{15}N-labled Trx-WW2 (*pink*). The overlay analysis showed that essentially all amide peaks originate from WW2 are distributed in a very narrow chemical shift window that is indicative of an unfolded protein.

(D) Overlay of the ^{15}N-HSQC spectrum of ^{15}N-labeled WW12 with that of ^{15}N-labled WW1, showing that the overall folding of WW1 in the WW12 tandem or alone are similar.

(E) ^{15}N-HSQC spectrum of ^{15}N-Kibra WW12 in complex with Dendrin PY23CT peptide. The assignments of the amide and Trp side chain peaks of Kibra WW12 are labeled.
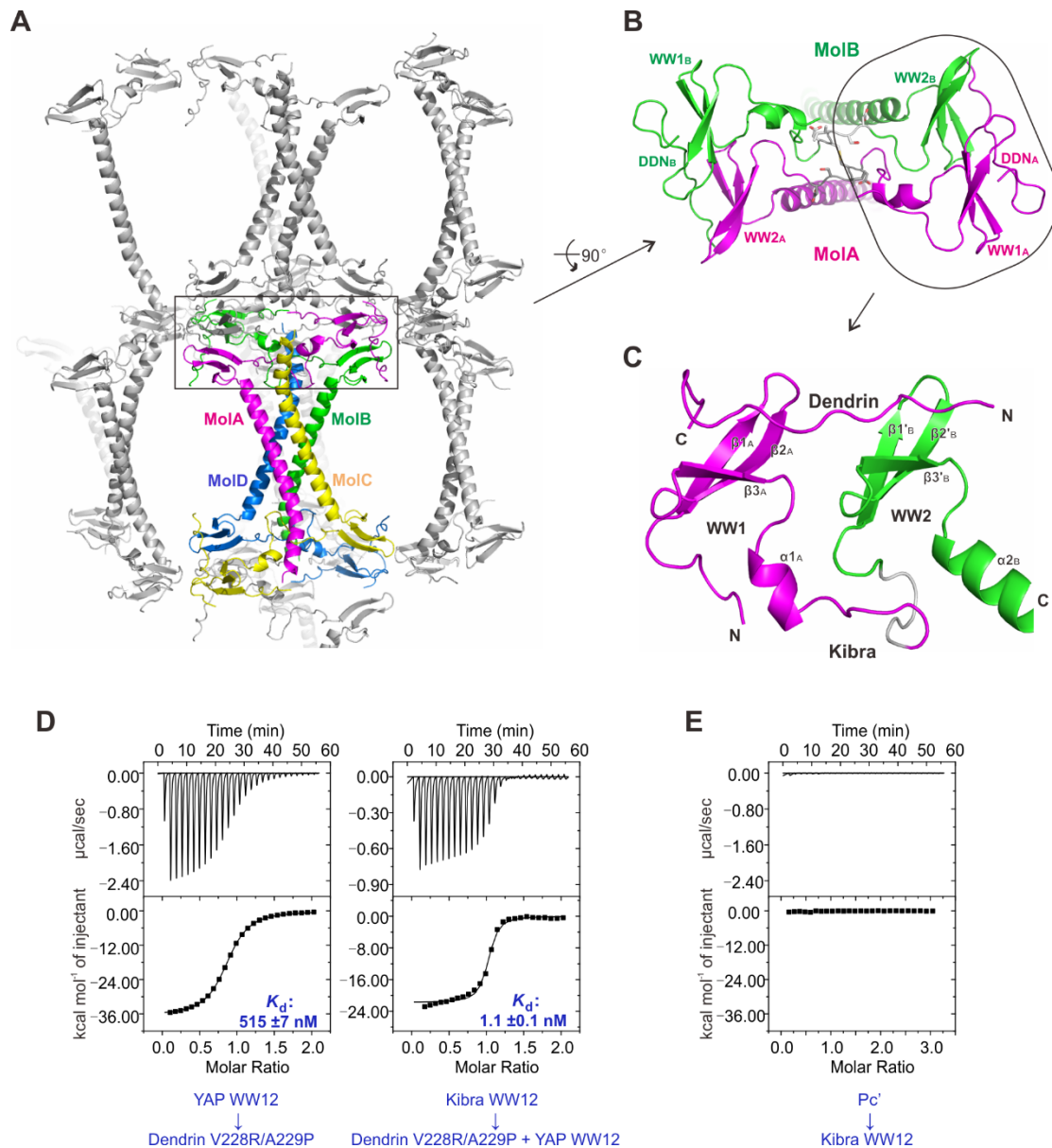
Figure S3. Crystal Structure of the Kibra WW12 /Dendrin PY23CT Complex. Related to Figure 2.

(A) Cartoon representation of the crystal packing of Kibra/Dendrin complex in the crystal. In this presentation, four complex molecules with a 4-fold rotational symmetry are colored in magenta, green, yellow and blue respectively.

(B) Cartoon representation of Kibra/Dendrin Molecular A and B forming domain-swapped dimer in the crystal. The swapping is mediated by residues from Asp49 to Asp53 (colored in *grey*).

(C) Cartoon representation of the rebuilt structure of Kibra/Dendrin heterodimer complex by converting the domain swapped Kibra WW12 tandem dimer into a monomer based on the observation that the Kibra WW12/Dendrin PY23CT complex forms a stable 1:1 monomer complex in solution (Figure 1D and E).

(D) (*Left*), ITC-based measurement of YAP WW12 binding to Dendrin PY23CT V228R/A229P. (*Right*), ITC-based measurement of Kibra WW12 binding to Dendrin PY23CT V228R/A229P saturated with 2-molar ratio of YAP WW12. Due to the super strong binding between Kibra WW12 and Dendrin PY23CT V228R/A229P, direct titration of Dendrin PY23CT V228R/A229P produced a

titration curve that could not be fitted to derive an accurate disassociation constant. To overcome this problem, a competition-based ITC (i.e. using the Kibra WW12 to compete with the weaker binder YAP WW12 shown in the *left panel*) was used to derive the reliable disassociation constant.

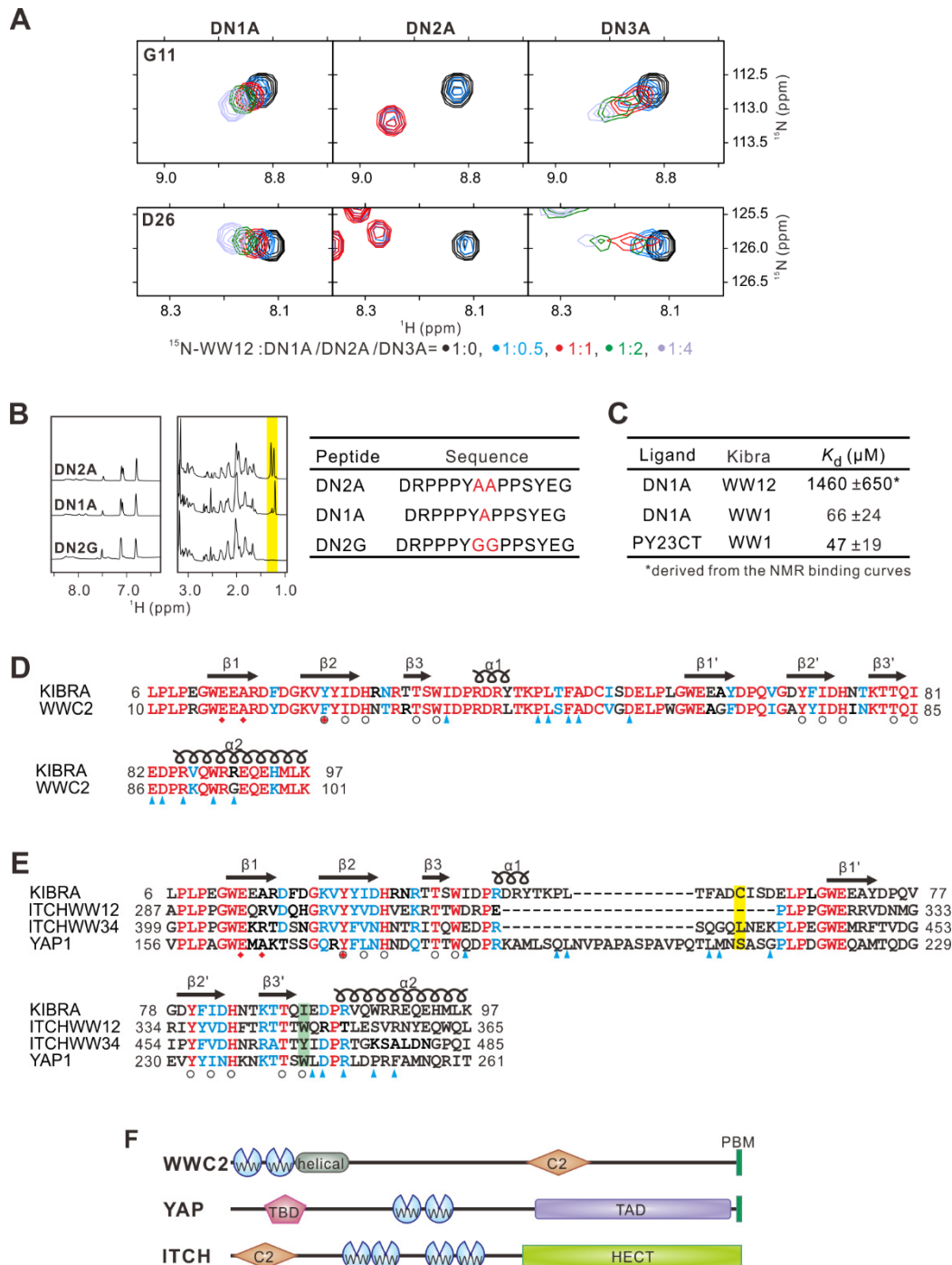(E) ITC-based assay showing that the cell-penetrating control peptide Pc' showed no detectable binding to Kibra WW12.

A

DN1A   DN2A   DN3A

G11

112.5
113.0
113.5
^{15}N (ppm)

9.0   8.8   9.0   8.8   9.0   8.8

D26

125.5
126.0
126.5
^{15}N (ppm)

8.3   8.1   8.3   8.1   8.3   8.1

^{1}H (ppm)

^{15}N-WW12 : DN1A /DN2A /DN3A = ● 1:0, ● 1:0.5, ● 1:1, ● 1:2, ● 1:4

B

DN2A
DN1A
DN2G

8.0 7.0   3.0 2.0 1.0
^{1}H (ppm)

Peptide	Sequence
DN2A	DRPPPYAAPPSYEG
DN1A	DRPPPYAPPSYEG
DN2G	DRPPPYGGPPSYEG

C

Ligand	Kibra	K_d (µM)
DN1A	WW12	1460 ±650*
DN1A	WW1	66 ±24
PY23CT	WW1	47 ±19

*derived from the NMR binding curves

D

β1   β2   β3   α1   β1'   β2'   β3'

KIBRA 6 LPLPEGWEEARDFDGKVYYIDHRNRTTSWIDPRDRYTKPLTFADCISDELPLGWEEAYDPQVGDYFIDHNTKTTQI 81
WWC2 10 LPLPRGWEEARDYDGKVFYIDHNTRRTSWIDPRDRLTKPLSFADCVGDELPWGWEAGFDPQIGAYYIDHINKTTQI 85

α2

KIBRA 82 EDPRVQWRREQEHMLK 97
WWC2 86 EDPRKQWRGEQEKMLK 101

E

β1   β2   β3   α1   β1'

KIBRA   6 LPLPEGWEEARDFDGKVYYIDHRNRTTSWIDPRDRYTKPL------------TFADCISDELPLGWEEAYDPQV 77
ITCHWW12 287 APLPPGWEQRVDQHGRVYYVDHVEKRTTWDRPE---------------------PLPPGWERRVDNMG 333
ITCHWW34 399 GPLPPGWEKRTDSNGRVYFVNHNTRITQWEDPR-------------------SQGQLNEKPLPEGWEMRFTVDG 453
YAP1   156 VPLPAGWEMAKTSSGQRYFLNHNDQTTTWQDPRKAMLSQLNVPAPASPAVPQTLMNSASGPLPDGWEQAMTQDG 229

β2'   β3'   α2

KIBRA   78 GDYFIDHNTKTTQIEDPRVQWRREQEHMLK 97
ITCHWW12 334 RIYYVDHFTRTTTWQRPTLESVRNYEQWQL 365
ITCHWW34 454 IPYFVDHNRRATTYIDPRTGKSALDNGPQI 485
YAP1   230 EVYYINHKNKTTSWLDPRLDPRFAMNQRIT 261

F

WWC2 WW WW helical   C2   PBM
YAP   TBD   WW WW   TAD
ITCH C2 WW WW WW   WW WW   HECT

Figure S4. Structural Determinants of the Kibra WW12/Dendrin PY23CT Binding. Related to Figure 3.

(A) Selected portions of ^{15}N-HSQC spectra of the ^{15}N-Kibra WW12 (*up*, G11; *down*, D26) showing during DN1A, DN2A or DN3A peptide titration, binding-induced chemical shift changes of the two selected residues. The titration experiments showed that WW12/DN2A underwent slow exchange indicative of strong binding, WW12/DN3A underwent intermediate to fast exchange indicative of relative weak binding and WW12/DN1A undergo fast exchange with minor chemical shift changes indicative of very weak binding.

(B) (*Left*), ^{1}H NMR spectra of peptide DN2A, DN1A and DN2G, showing that all these peptides are unstructured and have 2, 1, and 0 Ala as expected (Ala methyl group peaks highlight with *yellow* shading). This NMR-based analysis, together with the

mass spectrometry-based data, ensures the quality of the peptides used in our study. (*Right*), sequence of DN2A, DN1A, and DN2G peptides used in the current study.

(C) Summary table showing that isolate WW1 have similar binding affinity with DN1A and Dendrin PY23CT. Binding affinity between WW12 and DN1A were derived from the binding curves of 7 residues from the NMR titration experiments, and the rest were from ITC-based experiments.

(D) Structure-based sequence alignment of WW tandems from Kibra and WWC2. Totally conserved residues are colored in red and conserved residues are colored in blue. Key residues for WW12 supramodule coupling are labeled with *blue* arrows, residues for CT extension binding are labeled with *red* diamond and residues for canonical PY-motif interaction are labeled with circle.

(E) Structure-based sequence alignment of WW tandems from several WW domain containing proteins investigated in this study.

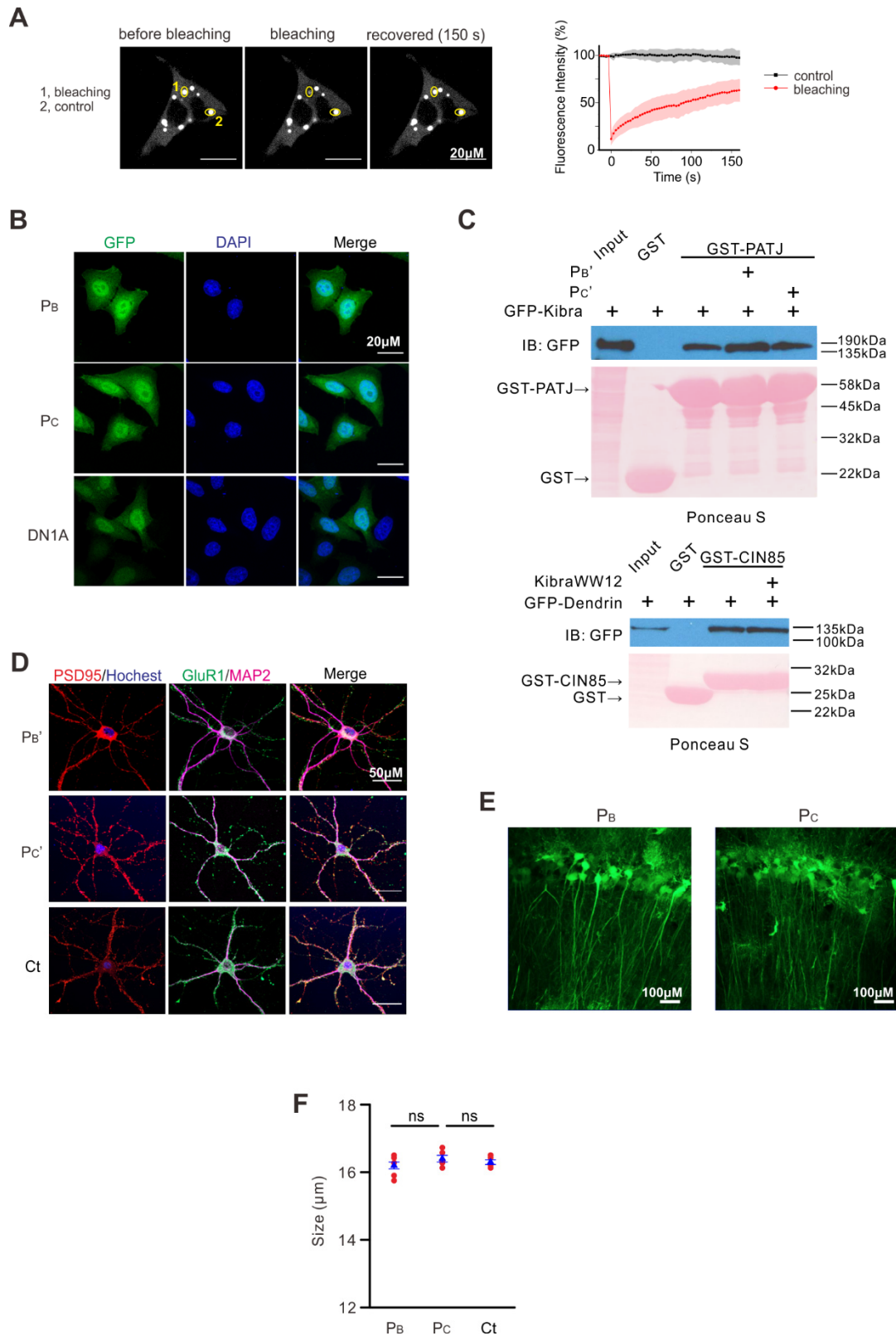(F) Domain organizations of the WW domain containing proteins used in ITC-based assays in Figure 3D.

Figure S5. Expression of Kibra WW12 Blocking Peptide. Related to Figures 4 and 5.

(A) Representative fluorescent images (*left*) of HeLa cells transiently expressing mCherry-Kibra, showing that the expressed Kibra formed puncta. The puncta formed by mCherry-Kibra appeared to be condensed liquid droplets, as the signal within the puncta could recover after photo-bleaching are graphed (*right*). The red

curve represents the averaged FRAP signal of 4 puncta bleached, and the black curve is the averaged fluorescent intensity of 4 control puncta. Time 0 refers to the time point of the photobleaching pulse. Intensities are normalized to the intensity at start point before bleaching. Data are mean ± SD.

(B) Representative fluorescent images of HeLa cells transiently expressing GFP- P_B, P_C or DN1A with nuclei stained with DAPI. All GFP-tagged peptide were dispersed in the whole cell with slightly nuclear enrichment.

(C) Pull-down experiments showing that cell-penetrating P_B' and P_C' peptide did not interfere with the Kibra-PATJ interaction and Kibra WW12 did not interfere with Dendrin-CIN85 interaction. (*Up*), GST-tagged PATJ PDZ8-10 could pull down GFP-tagged Kibra expressed in heterologous cells and addition of cell-penetrating P_B' or P_C' peptide did not affect the interaction. (*Down*), GST-tagged CIN85 SH3B could pull down GFP-tagged Dendrin expressed in heterologous cells and addition of purified Kibra WW12 did not affect the interaction.

(D) P_B peptide reduces the number of synaptic spines. The representative images show the cultured neurons (18DIV) without (Ct), or with treatment of P_B' or P_C' peptide at a concentration of 5 μM. The neurons were stained with antibodies against GluR1, PSD95 and MAP2 with nuclei stained with Hochest.

(E) Representative images showing the expression of P_C-GFP or P_B-GFP in the hippocampus of adult mice using the AAV-CAG-P_C-eGFP or AAV-CAG-P_B-eGFP vectors.

(F) Expression of P_B peptide does not alter the pyramidal cell size. The size of the individual pyramidal cells expressing control (Ct), P_C or P_B peptide and their averages per group (triangles) was measured. Data are mean ± SEM (n = 5 cells/group, ns: not significant, *t*-test). Related to Figure 4F
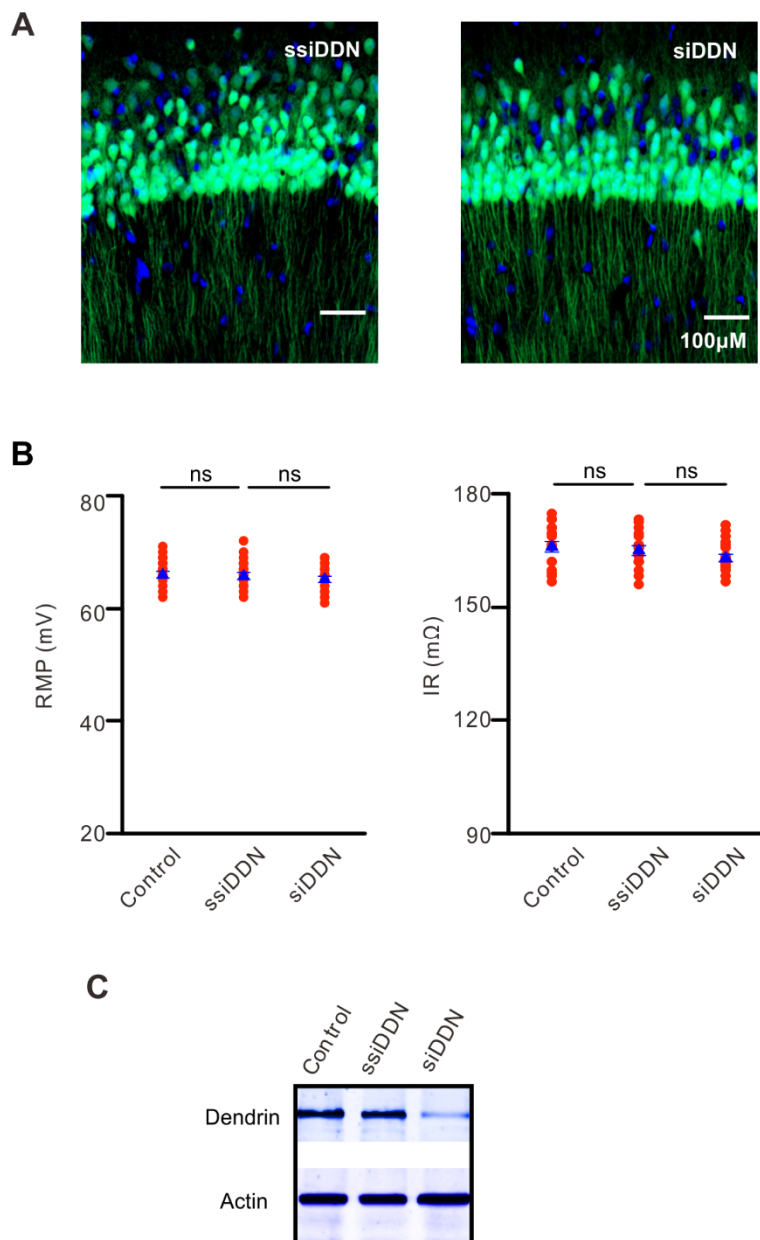
Figure S6. Silencing Dendrin Decreases Dendrin Protein Expression. Related to Figure 6.

(A) Representative images showing the expression of small interference RNA (siRNA) that specifically targets the Dendrin mRNA (DDN, siDDN) and a scrambled siRNA control (ssiDDN) in the CA1 hippocampus of adult mice using Lenti-U6-siDDN-eGFP and Lenti-U6-ssiDDN-eGFP virus.

(B) Both the resting membrane potentials (RMP) and input resistance (IR) in CA1 pyramidal neurons expressing siDDN were normal, as compared to those expressing control or ssiDDN. RMP was measured in the individuals (circles) and their averages per group with whole-cell patch clamp recordings immediately after breakthrough the cell membrane. IR was measured in the individuals (circles) and their averages per group (triangles) 30 min after the recordings of mEPSCs with intracellular solution containing potassium gluconate in Figure 6C. Data are mean ± SEM (n = 16 recordings/8 mice/group, ns: not significant, t-test).

(C) The siDDN, but not ssiDDN, decreases Dendrin protein expression. The cell lysates were prepared from the CA1 hippocampus of adult mice 4 weeks after injection of saline (control), ssiDDN or siDDN virus and blotted with antibodies against Dendrin and β-actin as indicated. The similar results were observed in four different experiments.
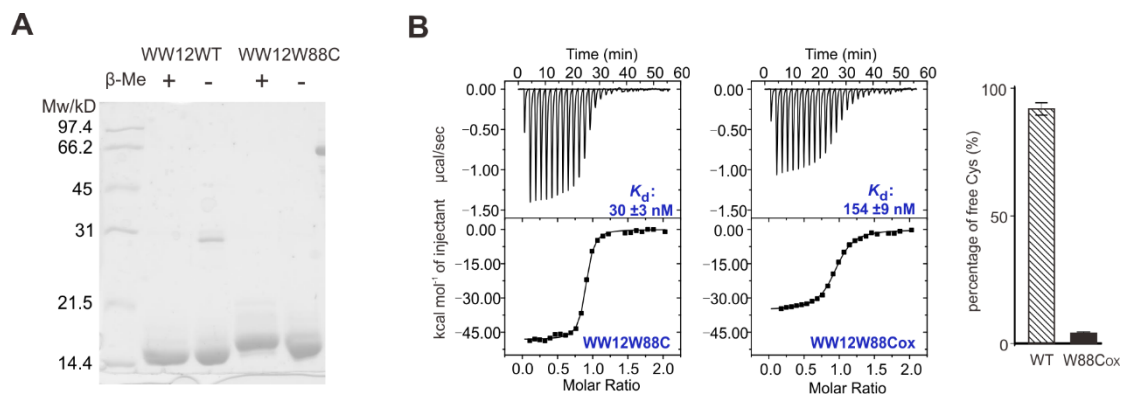
Figure S7. Oxidation of Kibra WW12W88C Weakens Its Binding to Dendrin. Related to Figure 7.

(A) Non-reducing SDS-PAGE analysis of WW12WT and WW12W88C purified with column buffer containing no DTT. WW12WT displayed a small fraction of intermolecular dimer band, as the protein only contains one Cys (C50). The Ellman assay also indicated that the majority of the WT WW12 was in the reduced form (*Panel B*, *right*). The WW12W88C only displayed as a monomer band but with obvious migration differences with and without the presence of β-mercaptoethanol in SDS-PAGE. The Ellman assay indicated that ~96% of WW12W88C was in the oxidized form when proteins were purified under the air oxidation condition (*Panel B*, *right*)

(B) ITC-based binding assay measuring the bindings of Dendrin PY23CT to reduced Kibra WW12W88C (reduced) or to oxidized Kibra WW12W88Cox (96% oxidized). The bar graph (*right*) compares the extent of air oxygen-mediated oxidation of Cys in WT Kibra WW12 and the WW12W88C mutant, showing that ~96% of Cys in WW12W88C was oxidized and only a very small fraction of Cys was oxidized in the WT WW12 when purified under the same condition. Data are mean ± SD from 3 repeats.

Table S1: Statistics of Data Collection and Model Refinement. Related to Figure 2 and Figure S3

	Kibra/Dendrin
Data collection	
X-ray source	SSRF
Space group	$P42_12$
Unit cell parameters (Å)	$a = b = 85.4$; $c = 80.6$
Resolution range (Å)	50-2.75 (2.80-2.75)
No. of unique reflections	8,167 (391)
Redundancy	12.5 (11.1)
I/σ	38.6 (2.8)
Completeness (%)	99.8 (99.0)
R_{merge} (%)[a]	7.1 (92.0)
Structure refinement	
Resolution (Å)	50-2.75 (3.15-2.75)
R_{cryst} / R_{free} (%)[b]	23.9/28.2
r.m.s.d bonds (Å) / angles (º)	0.011/1.2
Average B factor (Å^2)	47.7
No. of atoms	
Protein atoms	1,145
Water molecules	13
Ramachandran plot[c]	
Favored regions (%)	96.4
Allowed regions (%)	3.6
Outliners (%)	0

[a]$R_{merge} = \sum|I_i - I_m|/\sum I_i$, where I_i is the intensity of the measured reflection and I_m is the mean intensity of all symmetry related reflections.

[b]$R_{cryst} = \sum||F_{obs}| - |F_{calc}||/\sum|F_{obs}|$, where F_{obs} and F_{calc} are observed and calculated structure factors.

$R_{free} = \sum_T||F_{obs}| - |F_{calc}||/\sum_T|F_{obs}|$, where T is a test data set of about 5-10% of the total reflections randomly chosen and set aside prior to refinement.

[c]Defined by MolProbity (Chen et al., 2010).

Numbers in parentheses represent the value for the highest resolution shell.